Monthly Notices
of the
ROYAL ASTRONOMICAL SOCIETY
MNRAS **443,** 1463–1481 (2014) doi:10.1093/mnras/stu1213

Limitations in timing precision due to single-pulse shape variability in millisecond pulsars

R. M. Shannon,[1⋆] S. Osłowski,[2,3] S. Dai,[1,4] M. Bailes,[5] G. Hobbs,[1] R. N. Manchester,[1] W. van Straten,[5] C. A. Raithel,[6] V. Ravi,[1,7] L. Toomey,[1] N. D. R. Bhat,[8] S. Burke-Spolaor,[9] W. A. Coles,[10] M. J. Keith,[11] M. Kerr,[1] Y. Levin,[12] J. M. Sarkissian,[13] J.-B. Wang,[14] L. Wen[15] and X.-J. Zhu[15]

[1]*CSIRO Astronomy and Space Science, Australia Telescope National Facility, PO Box 76, Epping, NSW 1710, Australia*
[2]*Max-Planck-Institut für Radioastronomie, Auf dem Hügel 69, D-53121 Bonn, Germany*
[3]*Department of Physics, Universität Bielefeld, Universitätsstr. 25, D-33615 Bielefeld, Germany*
[4]*Department of Astronomy, School of Physics, Peking University, Beijing 100871, China*
[5]*Centre for Astrophysics and Supercomputing, Swinburne University of Technology, PO Box 218, Hawthorn, VIC 3122, Australia*
[6]*Department of Physics, Carleton College, Northfield, MN 55057, USA*
[7]*School of Physics, University of Melbourne, Parkville, VIC 3010, Australia*
[8]*International Centre for Radio Astronomy Research, Curtin University, Bentley, WA 6102, Australia*
[9]*Department of Astronomy, California Institute of Technology, Pasadena, CA 91125, USA*
[10]*Department of Electrical and Computer Engineering, University of California, San Diego, La Jolla, CA 92093, USA*
[11]*Jodrell Bank Centre for Astrophysics, University of Manchester, Manchester M13 9PL, UK*
[12]*School of Physics, Monash University, PO Box 27, Clayton, VIC 3800, Australia*
[13]*CSIRO Astronomy and Space Science, Parkes Observatory, PO Box 276, Parkes, NSW 2870, Australia*
[14]*Xinjiang Astronomical Observatory, Chinese Academy of Sciences, 150 Science 1-Street, Urumqi, Xinjiang 830011, China*
[15]*Department of Physics, University of Western Australia, Crawley, WA 6009, Australia*

Accepted 2014 June 12. Received 2014 June 12; in original form 2014 May 15

ABSTRACT

High-sensitivity radio-frequency observations of millisecond pulsars usually show stochastic, broad-band, pulse-shape variations intrinsic to the pulsar emission process. These variations induce jitter noise in pulsar timing observations; understanding the properties of this noise is of particular importance for the effort to detect gravitational waves with pulsar timing arrays. We assess the short-term profile and timing stability of 22 millisecond pulsars that are part of the Parkes Pulsar Timing Array sample by examining intraobservation arrival time variability and single-pulse phenomenology. In 7 of the 22 pulsars, in the band centred at approximately 1400 MHz, we find that the brightest observations are limited by intrinsic jitter. We find consistent results, either detections or upper limits, for jitter noise in other frequency bands. PSR J1909−3744 shows the lowest levels of jitter noise, which we estimate to contribute ∼10 ns root mean square error to the arrival times for hour-duration observations. Larger levels of jitter noise are found in pulsars with wider pulses and distributions of pulse intensities. The jitter noise in PSR J0437−4715 decorrelates over a bandwidth of ∼2 GHz. We show that the uncertainties associated with timing pulsar models can be improved by including physically motivated jitter uncertainties. Pulse-shape variations will limit the timing precision at future, more sensitive, telescopes; it is imperative to account for this noise when designing instrumentation and timing campaigns for these facilities.

Key words: methods: data analysis – stars: neutron – pulsars: general.

1 INTRODUCTION

Pulsar timing measurements enable the study of myriad phenomena of fundamental astrophysical and physical interest. These measurements, for example, have been used to characterize the orbits of binary systems, enabling tests of general relativity (Kramer et al. 2006), constraining nuclear equations of state (Demorest et al. 2010; Antoniadis et al. 2013), and detecting planetary-mass companions (Wolszczan & Frail 1992). By monitoring variations in pulse times of arrival (TOAs) from an ensemble of the most stable millisecond pulsars (MSPs) that have time-of-arrival precision of <100 ns, it is

⋆ E-mail: ryan.shannon@csiro.au

possible to detect the presence of nanohertz frequency gravitational radiation (Detweiler 1979; Hellings & Downs 1983). The ensemble is referred to as a pulsar timing array (PTA; Foster & Backer 1990). Current limits on gravitational radiation have been used to constrain the growth and evolution of black holes and their host galaxies in the low-redshift ($z \lesssim 1$) Universe (Shannon et al. 2013a). In order to detect gravitational waves it is necessary to improve the PTA data sets. This can be accomplished by (1) observing a larger set of pulsars; (2) increasing the observing span of the observations; and (3) increasing the quality of PTA data sets (Cordes & Shannon 2012; Siemens et al. 2013).

One of the most useful diagnostics for assessing the quality of a timing model is the pulsar timing residuals, which are the differences between the observed TOAs and a timing model (e.g. Edwards, Hobbs & Manchester 2006). It is well known that pulsar timing residuals show scatter in excess of what would be predicted by formal timing uncertainties (Groth 1975). This excess can be divided phenomenologically into at least two components; a time-correlated red-noise component and a white-noise component that is uncorrelated between observing epochs. The red noise can contain contributions from intrinsic spin noise (Shannon & Cordes 2010; Melatos & Link 2014), magnetospheric torque variations (Lyne et al. 2010), uncorrected dispersion variations (Keith et al. 2013), and multipath propagation effects (Cordes & Shannon 2010) in the interstellar medium, inaccuracies in terrestrial time standards (Hobbs et al. 2012), uncertainties in the Solar system ephemeris (Champion et al. 2010), the presence of asteroid belts (Shannon et al. 2013b), or other phenomena.

In addition to radiometer noise, white noise can originate from a number of sources. One of the most significant effect is associated with the difference between the ensemble-average pulse profile and the average of a finite number of pulses. The difference biases the measurements of arrival times, contributing *jitter* noise to the TOAs. Single pulses for nearly every pulsar observed with high sensitivity show variation in excess of that expected from radiometer noise. This includes variations in amplitude and phase that are correlated from pulse to pulse (such as the drifting subpulse phenomenon) and variations that are uncorrelated from pulse to pulse. If the jitter noise is independent from pulse to pulse (or decorrelates on a time-scale shorter than the time resolution of the observations), the root mean square (rms) error $\sigma_{\rm J}$ scales proportional to $\sigma_{\rm J}(N_{\rm p}) \propto 1/\sqrt{N_{\rm p}}$, where $N_{\rm p}$ is the number of pulses averaged in forming the integrated profile. The jitter noise is characterized either in terms of its rms contribution to the residual arrival times $\sigma_{\rm J}(N_{\rm p})$ or the dimensionless jitter parameter (Shannon & Cordes 2012):

$$f_{\rm J} \equiv \frac{\sigma_{\rm J}(N_{\rm p}=1)}{W_{\rm eff}}, \tag{1}$$

where $W_{\rm eff}$ is the intrinsic pulse width. Shannon & Cordes (2012) suggest multiplying the effective width by the factor $(1+m_{\rm I}^2)$, where $m_{\rm I}$ is the modulation index of the pulse energies. The motivation for including this factor is to distinguish variations in intensity from variations in shape (see Cordes & Shannon 2010; Shannon & Cordes 2012 for further discussion). The modulation index can be calculated from the mean $\mu_{\rm E}$ and standard deviation $\sigma_{\rm E}$ from the pulse-energy distribution:

$$m_{\rm I} = \frac{\sigma_{\rm E}}{\mu_{\rm E}}. \tag{2}$$

We consider different measurements of the effective pulse width, including both the full widths at 50 and 10 per cent of peak intensity (W_{50} and W_{10}, respectively) and effective widths that take into account the pulse shape. One measure of the effective pulse width that has been suggested (Downs & Reichley 1983; Cordes & Shannon 2010) is

$$W_{\rm eff} = \frac{\Delta\phi}{\sum_i [I(\phi_{i+1}) - I(\phi_i)]^2}, \tag{3}$$

where $\Delta\phi$ is the phase resolution of the pulse profile (measured in units of time), and the pulse profile is normalized to have a maximum intensity of unity. The denominator of equation (3) is proportional to the mean-squared derivative of the pulse profile and is therefore a measure of the sharpness of the pulse profile. Another measure of the effective pulse width that has been used (Liu et al. 2012) is

$$W_{\rm eff,L} = \frac{\int {\rm d}\phi\, \phi^2 I(\phi)}{\int {\rm d}\phi\, I(\phi)}. \tag{4}$$

In equations (3) and (4), $I(\phi)$ is the mean pulse profile as a function of pulse phase ϕ (measured in units of time).

Jitter noise is well known to be present in slower spinning pulsars (Helfand, Manchester & Taylor 1975; Cordes & Downs 1985) and is expected to be present in all pulsar observations when the single-pulse signal-to-noise ratio (S/N) exceeds unity (Osłowski et al. 2011; Shannon & Cordes 2012). Given the importance of precise timing to PTA experiments, a few recent studies have attempted to identify the presence of pulse jitter in MSPs. Using observations from the 64-m Parkes telescope at an observing frequency of ∼1400 MHz, Osłowski et al. (2011) investigated the timing precision limits in PSR J0437−4715, finding that in 1 h of observation, shape variations limit the timing precision to approximately 30 ns. Using observations from the Parkes telescope of PSR J0437−4715 at an observing frequency ∼1400 MHz, Liu et al. (2012) found a consistent level of jitter noise and estimated the jitter parameter to be $f_{\rm J} = 0.04$, based on the effective width defined in equation (4). Using observations from the 305-m Arecibo telescope at ∼1600 MHz, Shannon & Cordes (2012) connected single pulse variability in PSR J1713+0747 to high precision timing observations to find that jitter contributes ∼20 ns of timing uncertainty for an hour-duration observation.

The presence of jitter noise is connected to the stochasticity of single pulses. The single pulses of only three MSPs have hitherto been well characterized. Not surprisingly, these are three of the brightest MSPs at decimetre wavelengths: PSR J0437−4715 (Ables et al. 1997; Jenet et al. 1998; Osłowski et al. 2014); PSR J1939+2134 (Jenet, Anderson & Prince 2001; Jenet & Gil 2004); and PSR J1713+0747 (Shannon & Cordes 2012). Edwards & Stappers (2003) detected individual pulses in PSRs J1012+5307, J1022+1001, J1713+0747, and J2145−0750; however, only ∼100 pulses were detected for each pulsar and the statistics of the distribution of pulse energies were not explored. Additionally, Edwards & Stappers (2003) found evidence for quasi-periodic modulation of pulse intensities on time-scales of ∼10 pulse periods for PSRs J1012+5307 and J1518+4094. These quasi- periodicities were found not to dominate the single-pulse intensity modulation. In addition giant pulses, narrow pulses with energies that can be a factor of 40 greater than the mean pulse energy have been detected from PSR J1939+2134, PSR J1824−2452A, and PSR J1823−3021A (Knight et al. 2005).

While single-pulse variability is a nuisance for precision timing, it can be used as a tool to test models of the pulse emission mechanism. Cairns, Johnston & Das (2004) studied the phase-resolved single-pulse properties of two slower-spinning pulsars, PSRs B0950+08 and B1641−45, and interpreted these in the context of models of

pulsar emission. They found that over much of pulse phase, both pulsars showed log-normal energy distributions, and argued that stochastic growth, which predicts this type of distribution, plays the central role in the production of pulsar emission, in which linear instabilities in the plasma generate the radio emission. They contrast this theory to non-linear growth models which predict power-law energy distributions. Power-law energy distributions can also be produced from the vectorial superposition of two wave populations (Cairns, Robinson & Das 2002). Cairns et al. (2004) also found that near the edges of the pulse profile both pulsars showed Gaussian modulation, and suggested it was caused by either refraction in the magnetosphere, the superposition of many independent (log-normal) components, or was intrinsic to the emission mechanism.

Previous attempts to study single pulses and giant-pulse emission from MSPs have been limited by the low expected S/N for single pulses. Here we expand on previous studies to identify pulse-shape variations and assess the levels of jitter noise in the Parkes Pulsar Timing Array (PPTA) MSP sample (Manchester et al. 2013). Over the duration of the project, 22 MSPs have been regularly observed enabling us to measure or place limits on the levels of pulse jitter in these objects. The high cadence and long duration of the project have enabled us to select observations for which refractive and diffractive scintillation have significantly increased the observe flux density of the pulsars, enabling us to both detect single pulses and measure the effects of pulse jitter. In Section 2, we present the observations. In Section 3, the analysis methods that we use are discussed. In Section 4, we present results from the PPTA pulsars. In Section 5, we present a technique to correct TOA uncertainties for the effects of jitter noise. We apply this technique to a multiyear observations of PSR J0437−4715. We discuss and summarize our findings in Section 6.

2 OBSERVATIONS

For our analysis, we selected observations from the PPTA project, which includes observations of 22 MSPs south of a declination of $\approx+24^\circ$, the northern declination limit of the Parkes antenna. The pulsars are observed regularly, with an approximate observing cadence of 3 weeks, in three bands centred close to 730, 1400, and 3100 MHz, using the dual-band 10-cm/50-cm receiver and the central beam of the 20-cm multibeam receiver. In each of the bands, the observing bandwidth is 64, 256, and 1024 MHz, respectively. While the 20-cm system is typically the most sensitive to single pulses and pulse jitter, we also analysed observations obtained with the 10-cm/50-cm system to search for, or place limits on, these effects.

Most of the pulsars in the sample show large flux density variability at the PPTA observing frequencies due to diffractive and refractive interstellar scintillation (Rickett 1990). Diffractive interstellar scintillation causes pulsar radiation to show time and frequency variability in which the dynamic spectrum is broken up into scintles. Individual scintles show exponential distribution of intensity statistics and therefore have a long tail of rare but high intensities. In observing bands populated by few scintles, flux measurements show exponential or nearly exponential distribution in intensity. Refractive scintillation causes magnification (or de-magnification) of this pattern as detected at Earth, causing further variation in intensity. We find that some of the pulsars in the PPTA sample show measured intensities a factor of 20 greater than the mean. For these observations the Parkes observations have an S/N representative (or in excess) of the average observations of larger aperture telescopes such as the Green Bank Telescope and the expected observations from the MeerKAT telescope.

2.1 Fold-mode observations

In standard pulsar timing observations, spectra are formed and folded at the pulse period of the pulsar, as predicted by its ephemeris. For our observations, spectra were formed using both digital polyphase filter bank spectrometers (PDFB3 and PDFB4); and coherent dedispersion machines [CPU-driven ATNF Parkes Swinburne Recorder (APSR) and GPU-driven CASPER Parkes Swinburne Recorder (CASPSR)]. Observations of this type form the basis of the PPTA data set and comprise one component of the data analysed here. Individual subintegrations were of 8 or 32 s duration for CASPSR, and 60 s duration for the other backends. For further details see Manchester et al. (2013) and references therein.

Data calibration was conducted using standard data reduction tools (Hotan, van Straten & Manchester 2004b). To excise radio-frequency interference (RFI), we median filtered each subintegration in the frequency domain. The polarization was calibrated by correcting for differential gain and phase between the receptors through measurements of a noise diode injected at an angle of 45° from the linear receptors. In some observations with the 20-cm system, we corrected for cross-coupling between the feeds through a model derived from an observation of PSR J0437−4715 that covered a wide range of parallactic angles (van Straten 2004). However, we find that our results were independent of this cross-coupling calibration; this is because the effects of polarization are small compared the levels of jitter in our short ($\lesssim$1 h) observations that cover a small range in parallactic angle. The observations were then flux calibrated using observations of the radio galaxy Hydra A, which is assumed to have a constant flux and spectral index (Scheuer & Williams 1968).

We calculated TOAs by cross-correlating frequency-averaged observations with a template in the Fourier domain (Taylor 1992), which is presently the most common algorithm used for measuring arrival times. This algorithm assumes that the only source of noise in the measurement is white noise. The formal TOA uncertainties, Δ_F, are based on this assumption and therefore underestimate the true TOA uncertainty (Osłowski et al. 2011).

2.2 Baseband observations

We recorded raw-voltage (baseband) data for short intervals when pulsars were identified to be in particularly bright scintillation states. These intervals were identified in real time when the single-pulse S/N (measured by extrapolating from the fold-mode observations) significantly exceeded unity. Baseband data were recorded with the CASPSR instrument, which is capable of simultaneous real-time coherent dedispersion and baseband recording. Full Stokes single-pulse profiles were created by coherently dedispersing the baseband data off-line (van Straten & Bailes 2011) and calibrating for differential gain and phase of the feeds, and correcting for their cross-coupling where appropriate (van Straten 2013). These observations were not flux calibrated.

In Table 1, we summarize the seven single-pulse data sets used in this analysis. For all of the pulsars, between 40 000 and 300 000 pulses were observed. All of the single-pulse observations were obtained with the 20-cm system.

Table 1. Single-pulse observations.

PSR	P (ms)	S_{1400} (mJy)	MJD	N_p	⟨S/N⟩	S/N$_{max}$
J0437−4715	5.76	149	56446	1.0×10^5	16	89
J1022+1001	16.45	6	56304	3.8×10^4	1.8	9.9
J1603−7202	14.84	3	56409	4.2×10^4	1.6	11
J1713+0747	4.57	10	56447	1.1×10^5	1.9	7.5
J1744−1134	4.07	3	56514	6.1×10^4	3.1	11
J1909−3744	2.95	2	56310	3.9×10^5	2.2	11
J2145−0750	16.05	9	56206	4.3×10^4	5.5	22

Notes: For each pulsar, we list the period P of the pulsar, the flux density S_{1400} at a frequency of 1400 MHz, the MJD of the observation, the number of pulses obtained N_p, the average S/N (⟨S/N⟩), and the maximum S/N observed for a single-pulse S/N$_{max}$. The flux density measurements are from Manchester et al. (2013).

3 ANALYSIS METHODS

3.1 Timing analysis

Using the techniques described above, we derived TOAs from pulse profiles formed from $N_p = 1$ pulse to $N_p \sim 10^5$ pulses. For each pulsar, these TOAs were fitted to long-term timing models derived from PPTA observations (Manchester et al. 2013).

In some hour-duration fold-mode observations, we identified secular trends in arrival times. We attribute these trends to pulse-shape distortions caused by diffractive interstellar scintillation and intrinsic pulse profile evolution (Pennucci, Demorest & Ransom 2014). The diffractive scintillation pattern causes variable weighting of the pulse profile with frequency. If the pulse profile varies with frequency (as is common) the frequency averaged profile will change shape. We find that these trends could be adequately removed by re-fitting the timing model for pulsar spin frequency and frequency derivative. We defer discussion of the origin of these trends and methods for mitigation to future work.

To determine the level of jitter noise, we compared the measured rms of the residuals to levels expected from simulations of ideal data sets. In these simulated data sets, we formed pulse profiles from the template and white noise such that the S/N of each simulated subintegration matched the observed S/N.

We then define the rms uncertainty associated with jitter of N_p pulses averaged together, $\sigma_J(N_p)$ to be the quadrature difference between the rms of the observed and simulated data sets:

$$\sigma_J^2(N_p) = \sigma_{obs}^2(N_p) - \sigma_{sim}^2(N_p). \quad (5)$$

We assume here that all of the excess error in the arrival time measurements can be attributed to pulse jitter.

As discussed in Shannon & Cordes (2012), there are other perturbations to pulse arrival times that manifest on short (millisecond to hour) time-scales; however, very few effects can cause short time-scale distortions that depend at most weakly with frequency with the same strength in many backend instruments, at different telescopes, and at different observing frequencies, as is presented below. Distortions in pulse profiles caused by polarization calibration are likely to vary slowly with parallactic angle as receiver feeds rotate with respect to the pulsar (Stinebring et al. 1984). Distortions introduced at the telescope will be observatory dependent, backend dependent, or both. Similarly RFI will depend on the observing band and telescope site. By linking shape variations and timing variations on the shortest time-scales to timing variations on longer time-scales via equation (5) we estimate the contribution of jitter to TOA uncertainties.

We compared this to estimations for the level of jitter noise presented in Liu et al. (2012). Instead of using simulations to infer the levels of jitter σ_J, Liu et al. (2012) modify the TOA uncertainties $\Delta_{TOA,i}$, from the formal values Δ_F for $i = 1, N_{obs}$ using

$$\Delta_{TOA,i}^2 = \Delta_F^2 + \sigma_J'(N)^2, \quad (6)$$

and setting $\sigma_J'(N)$ to be the value at which the reduced χ^2 of the best-fitting model was unity. The jitter parameter is then calculated using equation (1). We obtained consistent results for $\sigma_J(N_p)$ using this method.

When we have single-pulse data sets, formal uncertainties on $\sigma_J(1)$ are small because there are many independent estimates of $\sigma_J(N_p)$. The uncertainty in $\sigma_J(1)$ cannot be derived from fitting the relationship $\sigma_J(N_p) = \sigma_J(1)/\sqrt{N_p}$ to a single data set and multiple N_p because $\sigma_J(N_p)$ are dependent and therefore their uncertainties are correlated. Instead it has to be derived from a single measurement of $\sigma_J(N_p)$ if only one data set is used. Alternatively it can be derived from multiple $\sigma_J(N_p)$ if independent data sets are used.

3.2 Pulse-shape analysis

The most direct way to link timing variations to shape variations is to analyse the properties of single pulses or subintegrations comprising as few pulses as feasible. In many observations, it was not possible to characterize every single pulse because of large variations in pulse amplitudes. The instantaneous S/N was typically ∼1–5; the pulsars show long positive tails of pulse energies in which the brightest pulses exceed the average pulse energy by a factor of 5.

While there are many established tools for analysing the properties of single pulses, central to our analysis is the measurement of the energy contained in a pulse or a subcomponent of a pulse. We define the energy of the pulse (or subcomponent) to be its integrated flux density. These included larger windows around the entire main pulse feature, subcomponents of the main pulse feature, precursor components, and interpulses. Regions around main pulses, precursors, or interpulses were set to contain more than 90 per cent of the pulse energy. Windows around other components were set to be centred on the component. If more than one subcomponent was measured for a pulsar, where reasonable, we chose windows of the same size to most directly compare the statistics of the individual components.

For each of the regions, we also defined an off-pulse window that was used as a control sample to assess the statistics of the noise in our measurements. The off–pulse windows were chosen to have the same width as the components of interest, and enabled us to empirically derive the noise statistics of the pulses. We normalized the measured energies by subtracting the off-pulse mean and then dividing by the off-pulse standard deviation. In our plots below, we therefore measure pulse energy in units of the S/N. Single pulses most severely affected by RFI showed anomalously high pulse energy and, by inspection, were removed from our sample. These were identified as containing non-dispersed impulsive signals that affected a larger range of pulse phase than the pulsar emission. In total, for each pulsar fewer than 10 pulses were removed, representing $\ll$0.1 per cent of the total pulse sample.

In order to assess the intrinsic energy distribution, it is necessary to deconvolve the effects of radiometer noise. Because the measured pulse energy is the sum of noise and the signal, the probability density function (PDF) for the measured energy ρ_E is the convolution of the PDFs of the noise (ρ_N) and intrinsic energy distribution (ρ_I):

$$\rho_E(E) = \int dE' \rho_N(E') \rho_I(E - E'). \quad (7)$$

We find, unsurprisingly, that the off-pulse distribution $\rho_{\rm N}(E)$ was very well modelled by a normal Gaussian.

We consider different models for the pulse-energy histogram based on generalized log-normal distributions and generalized Gaussian distributions. In most cases, we find that the pulse-energy histogram could be well modelled using a generalized log-normal distribution:

$$\rho_{\rm I}(E) = A \exp\left(-\left|\frac{\ln E - \ln \mu_{\rm E}}{\ln \sigma_{\rm E}}\right|^{\alpha}\right), \quad (8)$$

where A is a constant that normalizes the integral of the PDF to unity, and $\ln \mu_{\rm E}$, $\ln \sigma_{\rm E}$, and α parametrize the distribution. For $\alpha = 2$, equation (8) is a log-normal distribution.

As discussed below, one pulsar, PSR J1909−3744, shows a pulse-energy distribution with a shape that is better matched by a generalized Gaussian distribution. In this case, the pulse-energy distribution is modelled to be

$$\rho_{\rm L}(E) = A \exp\left(-\left|\frac{E - \mu_{\rm E}}{\sigma_{\rm E}}\right|^{\alpha}\right), \quad (9)$$

where A again is the normalizing constant, and $\mu_{\rm E}$, $\sigma_{\rm E}$, and α parametrize the distribution.

In order to find the best-fitting parameter values, we used a Metropolis–Hastings algorithm (Gregory 2005) to sample the parameter space using the likelihood function for the observed pulse energy given a set of model parameters.

In each bin ($i = 1, N$), centred at energy E_i and of width ΔE, the number of pulses is modelled to have multinomial probability; therefore, the logarithm of the likelihood function is

$$\log L = \log N! + \sum_{i}^{N} n_i \log p_i - \log n_i!, \quad (10)$$

where n_i is number of pulses detected in bin i, and p_i is the probability of finding a pulse in bin i.

Markov chains were used to sample the parameters $\boldsymbol{P} \equiv (\mu_{\rm e}, \sigma_{\rm E}, \alpha)$ for both the generalized log-normal and generalized Gaussian random variables. The Markov chain was computed using the standard procedure. At each step in the chain the likelihood $L_{\rm k}$ was calculated using equation (10). A provisional set of parameters $P'_{\rm k}$ were generated that were a perturbation on the previous parameters:

$$\boldsymbol{P}'_{\rm k} = \boldsymbol{P}_{\rm k} + \boldsymbol{\Delta P}. \quad (11)$$

The perturbation $\boldsymbol{\Delta P}$ was generated from a multidimensional Gaussian distribution with zero mean and variances set so that the acceptance rate (described below) was approximately 0.2–0.3. The likelihood function $L'_{\rm k}$ was calculated for these provisional values. If $L'_{\rm k} > L_{\rm k}$ the step was accepted. If $L'_{\rm k} < L_{\rm k}$ the step was accepted with probability $L_{\rm k}/L'_{\rm k}$.

After a burn-in period that is used to find the global maximum of the likelihood function, the Markov chain models the PDF of the parameters. For the best-fitting values we therefore take the mean of the Markov chain and for the parameter uncertainties we take the standard deviation of the Markov chain. We find that the resulting best-fitting distributions well modelled the pulse-energy distributions.

We used a χ^2 test statistic to assess the goodness of fit. For our histograms the test statistic is

$$\chi^2 = \sum_{i}^{N} \frac{(n - Np_i)^2}{Np_i(1 - p_i)}. \quad (12)$$

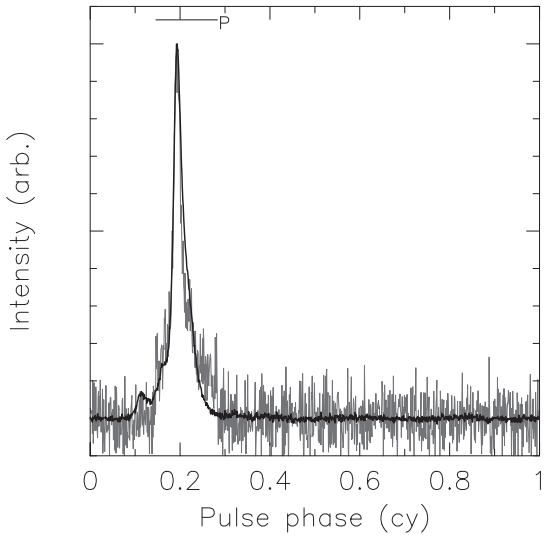

Figure 1. Pulse profiles for PSR J1713+0747. The thick line shows the average pulse profile for PSR J1713+0747, derived from averaging our single-pulse observations. The thinner grey line shows the pulse profile formed from 100 most energetic single pulses for PSR J1713+0747. The profiles have been normalized to have the same peak flux density. The horizontal line labelled P shows the pulse window used to measure pulse energy (see Fig. 2).

The denominator is the expected variance for bin i. The null hypothesis is that the data match the model. Under the assumption that the central limit theorem applies, the test statistic follows a χ^2 distribution with $N_{\rm dof} = N - N_{\rm fit}$ degrees of freedom, where $N_{\rm fit} = 3$ is the number of model parameters. If the fit is good, $\chi^2/N_{\rm dof} \approx 1$.

4 RESULTS

4.1 PSR J1713+0747

In an important test, our pulse-shape analysis of PSR J1713+0747 is consistent with a previous analysis presented in Shannon & Cordes (2012).

At 1400 MHz, the pulse profile of PSR J1713+0747, displayed in Fig. 1, is dominated by a 100 μs wide component flanked by broader emission. While the brightest single pulse has only an S/N of ≈10, the presence of the bright pulses is sufficient to distort averaged pulse shapes and induce excess scatter in the residual arrival times. The average pulse profile of the 100 brightest pulses is also displayed in Fig. 1. Compared to the average of all of the pulses, the profile is narrower with the peak of the profile located towards the leading edge of the average profile. The pulse width inferred from the average of all of the pulses is 110 μs, whereas the 50 per cent pulse width from the brightest pulses is ≈92 μs. When cross-correlating the brightest pulses with the average profile, we find that the bright profile is shifted early by 8.1 ± 0.1 μs. These results are consistent with observation of the correlation between S/N and early arrival time found by Shannon & Cordes (2012).

The energy distribution of single pulses, displayed in Fig. 2, shows that the pulse energies have approximately a log-normal energy distribution. The best-fitting model parameters for the pulse-energy distributions, for this and other pulsars, are displayed in Table 2. In particular we find that $\alpha \approx 1.4$, rather than 2 expected for a log-normal distribution. This energy distribution is in general

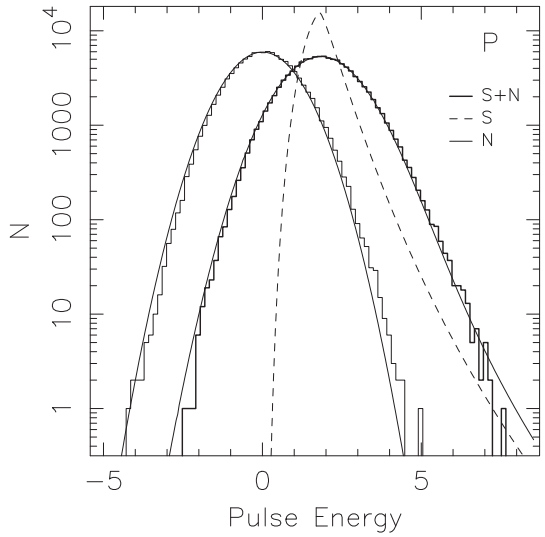

Figure 2. Pulse-energy histograms for PSR J1713+0747. The thick solid histogram shows the pulse-energy histogram in the on pulse window. The thick solid line (labelled S+N) is the best-fitting model to the distribution. The on pulse window is labelled P in Fig. 1. The thin solid histogram and line (labelled N) show, respectively, the histogram for the off-pulse window and the predicted normal Gaussian distribution. The units of pulse energy have been scaled to the rms of the off-pulse window. The thin dashed line (labelled S) shows the intrinsic pulse-energy histogram, deconvolved using equation (7).

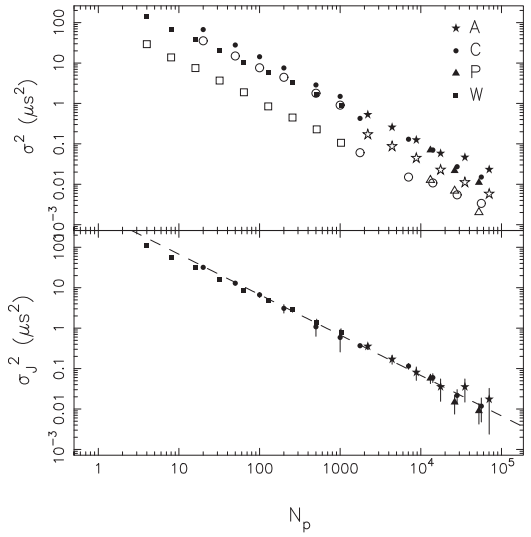

Figure 3. Estimates of jitter noise in PSR J1713+0747. Upper panel: variance of residual time series versus number of pulses averaged N_p for observations (filled symbols) and simulated data sets (open symbols) from observations with the Parkes telescope and the Arecibo telescope. Because the data were obtained with telescopes with different sensitivities, the observed and simulated time series contain different levels of white noise. Lower panel: $\sigma_J(N_p)$, the quadrature difference between the observed and simulated data sets. The dashed line is the best-fitting model for the jitter noise scaling $\propto N_p^{-1/2}$. Symbols: squares – Arecibo/WAPP Observations (labelled W, autocorrelation spectrometer) observing at 1600 MHz; stars – Arecibo/ASP (labelled A, a coherent dedispersion machine, using single channel of 4 MHz of bandwidth) observing at 1400 MHz ; circles – Parkes/CASPSR observing at 1400 MHz (labelled C); triangles – Parkes/PDFB4 observing at 1400 MHz (labelled P).

agreement with observations made in the same frequency band by Shannon & Cordes (2012). Based on the model energy distribution we find that the modulation index is $m_I \approx 0.3$ averaged over a window encompassing most of the pulse energy. While this is a borderline value for Gaussian intensity modulation (McKinnon 2004), the pulse-energy statistics clearly depart from Gaussianity.

In Fig. 3, we compare estimates of the levels of jitter $\sigma_J(N_p)$ from these Parkes observations to the previous Arecibo observations (Shannon & Cordes 2012). While the observations show different levels of total timing error, displayed in the upper panel of Fig. 3, this is entirely due to the different sensitivity of the observing systems and the scintillation state of the pulsar at the epochs of observation. After subtracting the contribution associated with radiometer noise, the excess noise can be modelled using a single power law, shown

Table 2. Models for pulse-energy distributions in PPTA pulsars.

PSR	Comp	μ_E	$\ln \sigma_E$	α	m_I	χ^2/N_{DOF}
		Generalized log-normal distribution				
J0437−4715	P	14.47(1)	0.303(2)	1.645(7)	0.390(8)	61.6
	C1	18.24(2)	0.586(3)	1.884(9)	0.694(2)	51.3
	C2	3.350(1)	0.197(3)	1.142(8)	0.493(1)	18.3
J1022+1001	P	1.623(1)	0.5023(6)	2.20(9)	0.4859(5)	0.9
	C1	1.123(3)	0.518(4)	2.19(3)	0.506(3)	0.8
	C2	0.794(6)	1.136(7)	2.86(3)	0.958(3)	1.2
J1603−7202	P	1.398(2)	0.595(1)	2.392(5)	0.543(1)	1.5
	C1	0.674(1)	1.420(2)	3.161(9)	1.156(1)	1.8
	C2	0.728(2)	1.136(2)	3.39(1)	0.852(7)	1.0
J1713+0747	P	1.821(1)	0.1715(5)	1.334(2)	0.2870(2)	2.0
J1744−1134	P	2.836(4)	0.459(6)	2.69(6)	0.388(2)	1.7
J2145−0750	P	5.276(5)	0.2286(8)	1.589(6)	0.3003(8)	8.7
	C1	3.930(5)	0.677(2)	2.44(1)	0.617(1)	1.6
	C2	2.376(5)	0.490(7)	2.45(5)	0.433(2)	0.9
PSR	Comp	μ_E	σ_E	α	m_I	χ^2/N_{DOF}
		Generalized normal distribution				
J1909−3744	P	0.408(3)	4.345(3)	4.275(8)	0.627(2)	33.1

Notes: Numbers in parentheses are the uncertainty in the last digit of the parameters, and are derived from Monte Carlo simulation (see text).

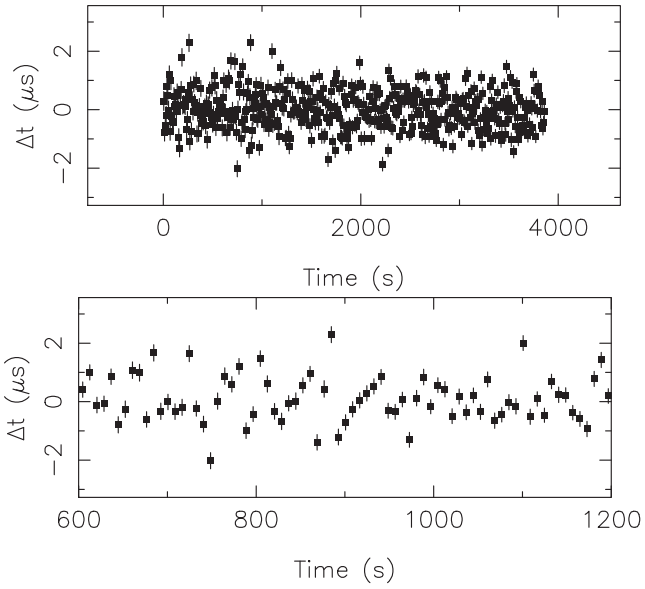

Figure 4. Top panel: residual arrival times for 3840 s observation of PSR J1713+0747, derived from CASPSR observations with 8 s subintegrations. Bottom panel: subinterval highlighting drift in arrival times over ∼48 s at a time of 900 s.

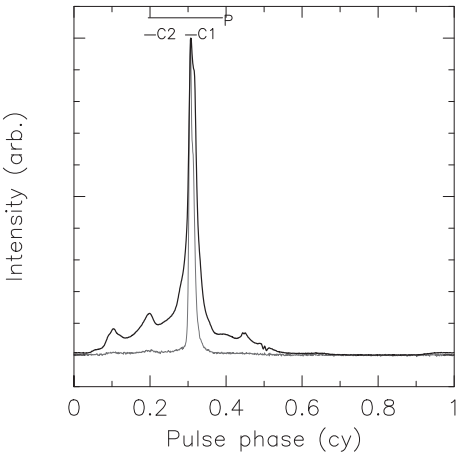

Figure 5. Pulse profiles for PSR J0437−4715. The thick line shows an average pulse profile for PSR J0437−4715 formed from all of our single-pulse observation. The thinner grey line shows the profile formed from 100 most energetic pulses. The profiles have been normalized to have the same peak flux density.

in the bottom panel of Fig. 3. We emphasize again that the previous study utilized observations from the Arecibo telescope and two backends with markedly different architectures than the ones used here: including an autocorrelation spectrometer and a CPU-based coherent dedispersion machine with lower frequency resolution. Based on both analyses we expect jitter to contribute ∼25 ns of rms uncertainty to an hour-long observation of PSR J1713+0747.

We were able to detect jitter noise in PSR J1713+0747 at 3100 MHz using only fold-mode observations. We find that the rms contribution of jitter noise was similar at 1400 and 3100 MHz. At these frequencies the average pulse profiles have similar widths. We did not detect jitter noise in 730 MHz observations. Our limit level of jitter noise is larger, and hence consistent with the measured level in the higher frequency observations.

We also find evidence for time-correlated structure in the residuals. In the brightest CASPSR fold-mode observation at 1400 MHz, the residuals occasionally show monotonic drifts across ∼1 μs over ∼48 s. In Fig. 4, we show the residual arrival times for both the entire ∼3800 s observation and a subsection showing an apparent drift. The drifts are correlated between both the top half of the subband, indicating that pulse profile evolution modulated by the dynamic spectrum is not causing this effect. One other pulsar, PSR J1909−3744 shows structure in the residuals, with a different magnitude on a shorter time-scale. This is discussed further below. Other pulsars, with comparable or better timing precision, such as PSR J0437−4715 discussed below, do not show a drift like this, suggesting that the effect is not associated with the backend instrumentation or data analysis. We were unable to detect this effect in other backend instrumentation because of insufficient time resolution. This emission could possibly be associated with the drifting subpulse phenomenon, observed in many slower pulsars, in which bright emission gradually moves through the pulse profile, with an inferred drift rate of $\ll$0.1 cycles per pulse period. It could also be aliased from a much higher drift rate. If unaliased, the inferred drift rate is lower by at least six orders of magnitude than that observed in slower pulsars. This drifting is subdominant to the random white-noise component to pulse jitter.

4.2 PSR J0437−4715

At decimetre wavelengths, PSR J0437−4715 is the brightest known MSP, with a phase-averaged flux density of 150 mJy at 1400 MHz. Because of its high flux density, pulse-shape variations cause timing uncertainty that is at least a factor of 8 greater than that expected from radiometer noise (Osłowski et al. 2011). Its single pulses have been widely studied (see references above).

At 1400 MHz, the pulsar has detectable emission over more than 85 per cent of pulse phase. The average pulse profile, displayed in Fig. 5, shows many components but is dominated by a central peak. In Fig. 5, we also show a pulse profile formed by averaging the 100 most energetic pulses. The 50 per cent pulse width of the average of the brightest pulses is 80 μs, which is significantly narrower than the 140 μs width of all of the pulses. These are consistent with observations presented in Osłowski et al. (2011).

For PSR J0437−4715, we analysed windows encompassing most of the pulse energy centred on the main peak (labelled P in Fig. 5) and narrower windows centred on the main peak and two of the leading subcomponents. The pulse-energy distributions for emission in windows P, C1, and C2 are displayed in Fig. 6. We find that for all three components, the pulse shows approximately log-normal pulse-energy distribution, though the best-fitting models, listed in Table 2, are the worst matching of all of the pulsars in our sample. For windows P and C1, we find an excess of intermediate-strength pulses. Based on the calculations of models of pulse energy we find that the modulation index m_I for the components varies from 0.3 to 0.7 with the modulation index over the widest window being 0.4. We searched for, but did not find evidence of, correlations in energy between the different windows.

Like PSR J1713+0747, we determined the level of jitter noise $\sigma_J(N_p)$ for PSR J0437−4715. The results of this analysis are presented in Fig. 7. We find that both the total timing error and $\sigma_J(N_p)$ scale proportionally to $N_p^{-1/2}$ for integrations comprising 1–10^5 pulses. The levels of jitter are consistent in observations at different epochs. At 1400 MHz, we find that jitter contributes ≈40 ns (rms) to the residuals for an hour-duration observation, which is consistent

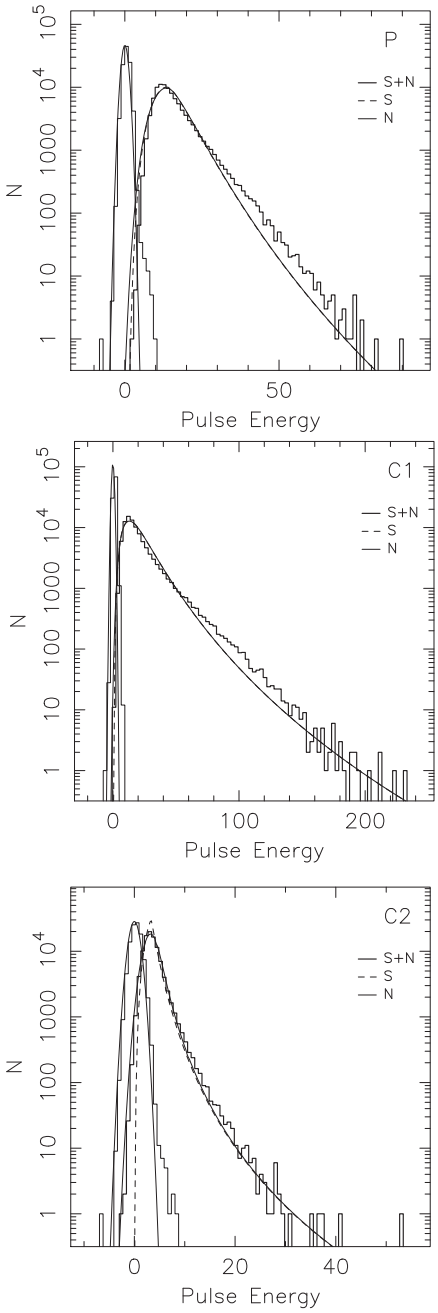

Figure 6. Pulse-energy histograms for PSR J0437−4715. The uppermost panel shows the histogram for a window containing the brightest part of the pulse profile (labelled P in the upper panel of Fig. 5), the middle panel shows the distribution for a window centred on component C1, and the lowermost panel shows the distribution for a window centred on component C2. The labels are the same as in Fig. 2.

with previous estimates for the level of jitter noise for this pulsar (Liu et al. 2012).

The level of jitter noise is modestly smaller at higher frequency and modestly greater at lower frequencies. This is likely related to the narrowing of the pulse width at higher frequencies.

Because of the high flux density of the pulsar, all observations in all three bands are jitter dominated. It is possible to measure the effects of jitter simultaneously with the 10-cm/50-cm system and assess the degree of correlation between the bands. In the upper and middle panels of Fig. 8, we show the correlation between residual

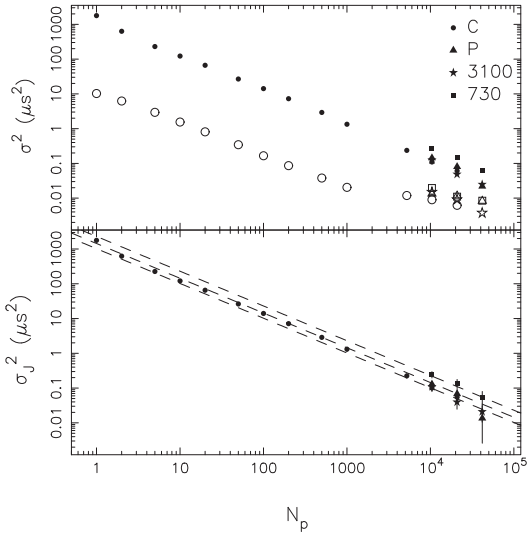

Figure 7. Estimates for levels of jitter noise in PSR J0437−4715. Upper panel: variance of residual time series for observed data sets (filled symbols) and simulated data sets (open symbols) from observations with the Parkes telescope. Lower panel: the quadrature difference between the observed and simulated data sets, $\sigma_J(N_p)$. Symbols: squares – 50-cm/PDFB3 observations at 730 MHz (labelled 730); stars – 10-cm/PDFB4 observations observing at 3100 MHz (labelled 3100); circles – Parkes/CASPSR observing at 1400 MHz (labelled C); triangles – Parkes/PDFB4 observing at 1400 MHz (labelled P). The top dashed line shows the fitted jitter model for the 50-cm data. The middle dashed line shows the fitted jitter noise to the 20-cm data. The bottom dashed line shows the fitter jitter model for the 10-cm observations.

TOAs formed from the upper and lower halves of the 10- and 50-cm, observations respectively. We find that there is a high level of correlation between residuals. Within the 50-cm band we find that the correlation coefficient is 0.7. The probability of the null hypothesis (that there is no correlation) is 3×10^{-17}, indicating that the correlation is highly significant. Within the 10-cm band we find that the correlation coefficient is 0.8. The probability of the null hypothesis is 1×10^{-15}, again indicating that the correlation is highly significant. In the bottom panel of Fig. 8, we plot residuals formed from the nearly simultaneous observations with the 10- and 50-cm system. The start times for the observations were different in the bands by 1 s, which should decorrelate the residuals TOAs by only a small amount because profiles are formed from 60 s subintegrations. The correlation coefficient for the residuals TOAs in both bands is found to be 0.2. The probability of no correlation is also 0.2, indicating that there is no evidence for correlated TOAs. We therefore place a limit on the jitter bandwidth of $\lesssim$2 GHz. We attempted to form TOAs in finer subbands of the 3100 MHz system, in order to assess if there is a loss of correlation over the 1024 MHz band of the system. We find no evidence for a decorrelation.

4.3 PSR J1022+1001

PSR J1022+1002 is a relatively bright (6 mJy phase-averaged flux density) pulsar with a 16 ms spin period. It scintillates strongly at 1400 MHz, enabling studies of pulse-shape changes and short-term timing variations with the Parkes telescope. Previous timing analysis at both Parkes and other observatories shows that PSR J1022+1002 has timing variations well in excess of those expected from radiometer noise. This excess has been attributed to long-term pulse profile instabilities (Kramer et al. 1999) and imperfect polarization

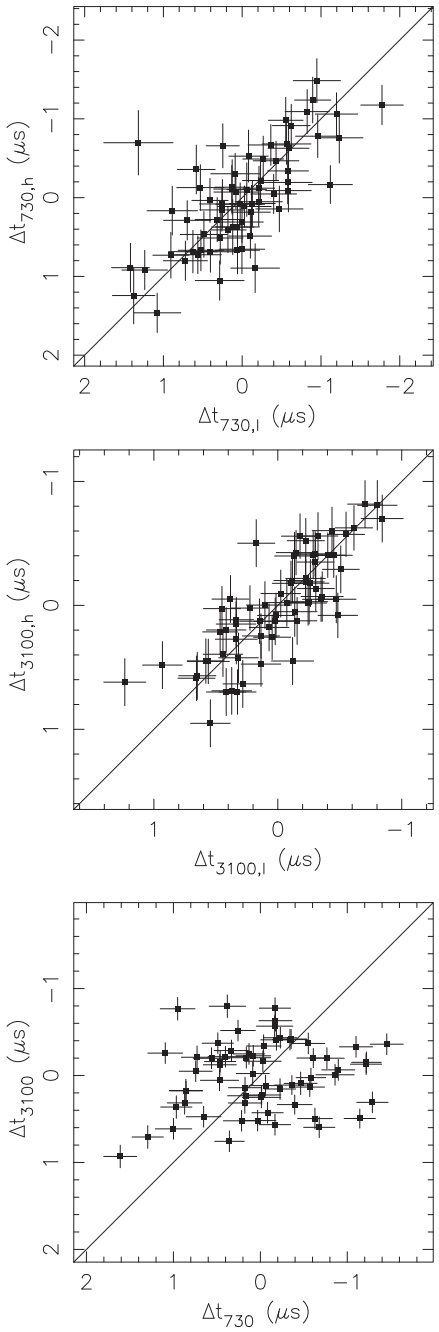

Figure 8. Correlation of residual TOAs for PSR J0437−4715. In the uppermost panel, we show the correlation between residuals formed from the lower half $\Delta t_{730,l}$ and upper half $\Delta t_{730,h}$ of the 730 MHz (50 cm) band. In the middle panel, we show the correlation between residuals formed from the lower half $\Delta t_{3100,l}$ and upper half $\Delta t_{3100,h}$ of the 3100 MHz (10 cm) band. In the bottom panel, we plot residuals formed at 730 MHz (Δt_{730}) and 3100 MHz (Δt_{3100}) observations. In all the panels, the solid lines denote unit correlation.

calibration (Hotan, Bailes & Ord 2004a; van Straten 2013). Here we identify a component of this excess associated with single-pulse variability.

At 1400 MHz, the profile of PSR J1022+1001, displayed in Fig. 9, is dominated by two components. In our analysis of pulse energy we measured the pulse energy from a window encompassing most of the main pulse (labelled P in Fig. 9) and windows centred

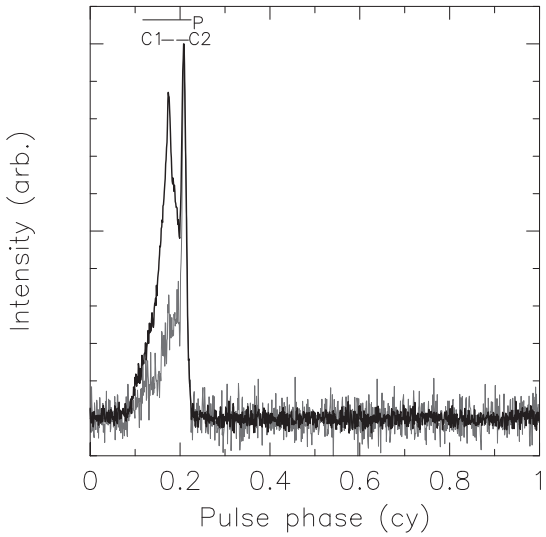

Figure 9. Pulse profiles for PSR J1022+1001. The thick line shows the average pulse profile formed from all of our single-pulse observations. The thinner grey line shows the average of the 100 brightest pulses. The profiles have been normalized to have the same peak flux density.

on the dominant leading (labelled C1) and trailing (labelled C2) components. The dominant components have approximately the same total intensity. The trailing component is nearly 100 per cent linearly polarized, whereas the leading component shows relatively low levels of polarization. The pulse profile formed from the brightest 100 pulses is also displayed in Fig. 9. While bright individual pulses are found to be centred on both components C1 and C2, the majority of the brightest pulses originate from C2. In the profile formed from the brightest pulses, component C1 is approximately five times weaker than component C2.

The pulse-energy distribution for PSR J1022+1001, and its subcomponents, displayed in Fig. 10, show log-normal distributions.

The best-fitting models for the pulse-energy distributions are listed in Table 2. The window around the leading component C1 has a larger mean energy, but a lower intensity modulation than the window around component C2, consistent with observation that the bright pulses are dominated by the second component. We find no evidence for correlations in the energies of components C1 and C2.

When calculating the levels of jitter noise, we find that $\sigma_J(N_p) \propto N_p^{-1/2}$ with consistent levels of jitter noise inferred from different backends. In 1 h of observations we estimate that jitter noise contributes ≈280 ns rms noise to the observations at 1400 MHz. At 3100 MHz we find comparable levels of pulse jitter noise to that measured at 1400 MHz. At 730 MHz, we find that the level of pulse jitter was less than that measured at higher frequency.

Polarization calibration and pulse profile evolution also cause measurable pulse-shape changes for this pulsar, and have previously limited its timing precision. Because of the high level of linear polarization of narrow component C2, PSR J1022+1001 is especially susceptible to polarization calibration errors. In an analysis of 5 yr of observations of this pulsar van Straten (2013) showed that improper polarization could contribute ∼800 ns of excess (rms) scatter to the residual arrival times. The pulsar shows significant pulse profile evolution, with the leading component C1 having a large spectral index. At 1400 MHz, the pulsar scintillates strongly, and the combination of pulse profile evolution and scintillation can cause significant variations in the frequency-averaged pulse profile.

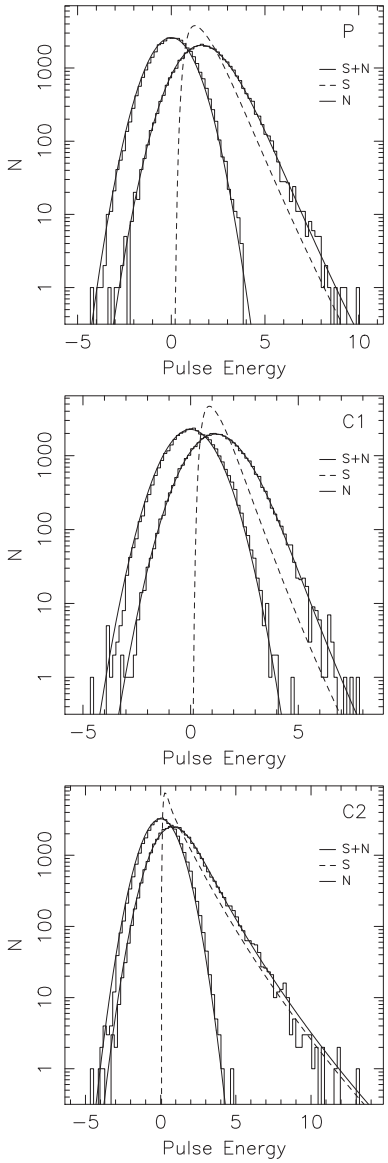

Figure 10. Pulse-energy distributions for PSR J1022+1001. In the uppermost panel, we show the energy distribution over the majority of the pulse (window P in Fig. 9), in the middle panel we show the energy distribution for a window C1 centred on the leading component, and in lowermost panel we show the energy distribution in a window C2 centred on the trailing component. The labels are the same as in Fig. 2.

Both of these effects are correctable; if these effects are corrected jitter noise will limit the achievable timing precision for this pulsar.

4.4 PSR J1603−7202

PSR J1603−7202 has a spin period of ∼15 ms. At 1400 MHz, the profile of PSR J1603−7202, displayed in Fig. 11, is dominated by two components connected by a bridge of emission. We measured pulse energies in a window containing most of the main pulse (labelled P in Fig. 11), and smaller windows centred on two dominant subcomponents (labelled C1 and C2). The pulse profile formed from the 100 brightest pulses is also displayed in Fig. 11. While the brightest individual pulse, integrated over the full window, was dominated by the trailing component C2, the vast majority of the

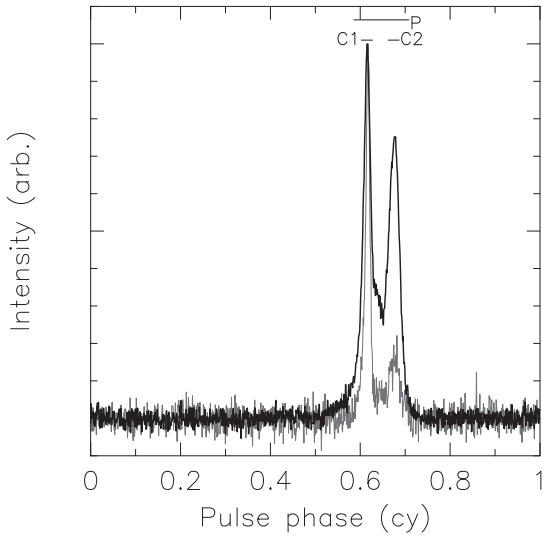

Figure 11. Pulse profiles for PSR J1603−7202. The thick line shows the average pulse profile formed from all of our single-pulse observations. The thinner grey line shows the average of the 100 brightest pulses. The profiles have been normalized to have the same peak flux density.

bright pulses, and the brightest pulses in narrower windows tended to originate from component C1.

The pulse-energy distribution, displayed in Fig. 12, shows evidence for approximately log-normal statistics over in the windows containing the main pulse and components C1 and C2. Window C1, containing the leading component, has a lower mean energy, but a higher variance (and hence higher modulation index) than window C2, which contains the trailing component. The best-fitting models for the pulse-energy distributions are presented in Table 2. We find no evidence for correlation between the components C1 and C2.

When calculating the level of jitter noise, we find $\sigma_J(N_p) \propto N_p^{-1/2}$ and we estimate that in a 1 h observation at 1400 MHz that jitter induces an rms error of ≈200 ns. We were unable to detect the presence of jitter noise at other frequencies, but the upper limits were consistent with the 1400 MHz observations.

4.5 PSR J1744−1134

PSR J1744−1134 has a relatively narrow main pulse and a faint interpulse, as displayed in the upper panel of Fig. 13. The pulsar has a spin period of ∼4.1 ms. While it has a flux density of only 3.1 mJy, it scintillates strongly at 1400 MHz.

We have identified single-pulse emission from the main pulse but do not detect strong pulses from the interpulse. The average profile of the 100 brightest pulses, also displayed in the upper panel of Fig. 13, is consistent in width with the average of all the pulses, suggesting that bright pulses are emitted over a wide range of pulse phase. We calculated the pulse-energy distribution in window P (see Fig. 13) containing the majority of the energy of the main pulse. We find that the pulse-energy distribution in this window, displayed in the bottom panel of Fig. 13, shows an approximately log-normal energy distribution.

Like the majority of pulsars in our sample we find that $\sigma_J(N_p) \propto N_p^{-1/2}$ up to $N_p = 6 \times 10^4$, the largest value we searched. Based on these results we estimate that in 1 h of observation jitter noise contributes ≈40 ns rms error to the arrival times for observations close to 1400 MHz. The low levels of jitter noise are attributed to the relatively narrow pulse profile. For this pulsar we were unable

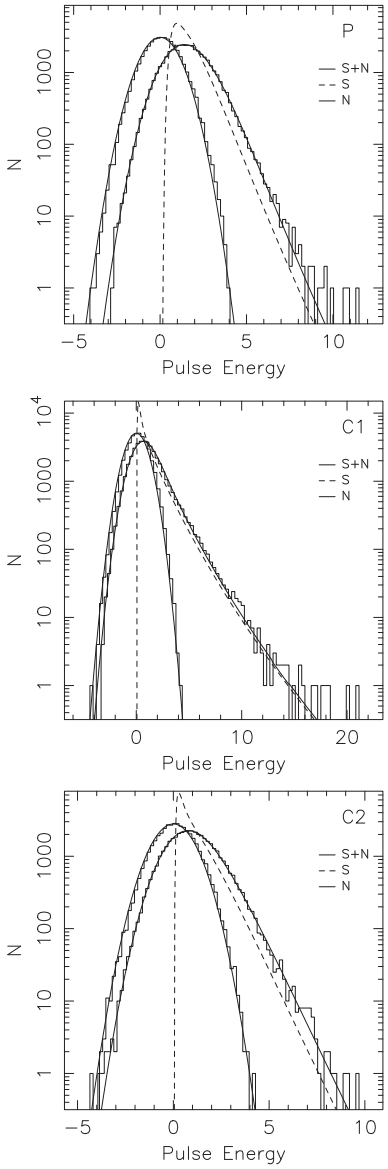

Figure 12. Pulse-energy histograms for PSR J1603−7202. In the uppermost panel, we show the pulse energy measured in window P containing most of the pulse profile, as identified in the uppermost panel of Fig. 11. In the middle and lowermost panels, we show the pulse energy measured in windows C1 and C2, also identified in Fig. 11, which are centred, respectively, on the two leading and trailing components of the pulse profile. The labels are the same as in Fig. 2.

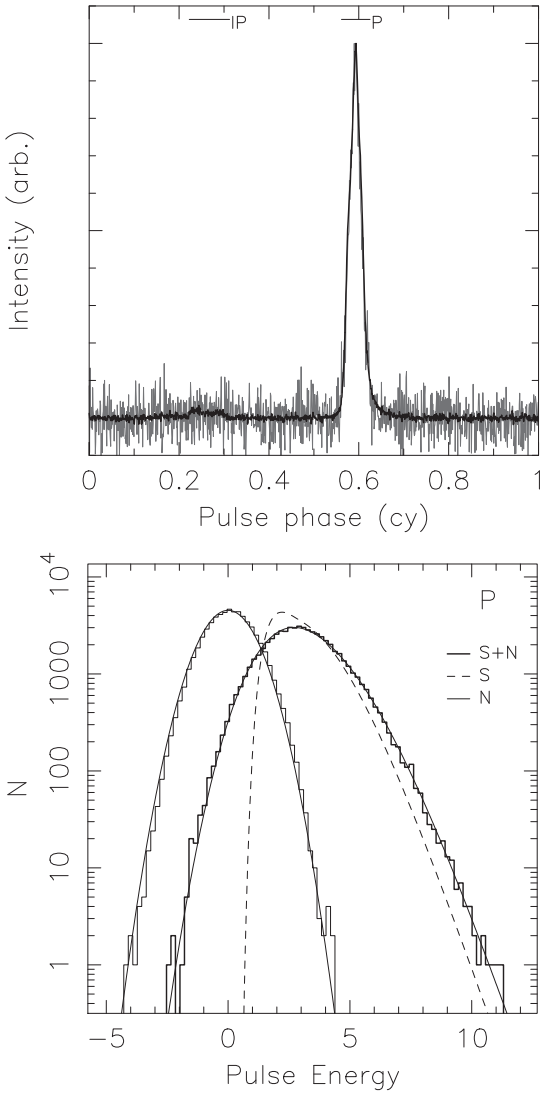

Figure 13. Top panel: pulse profiles for PSR J1744−1134. The thick line shows the average pulse profile formed from all of our single-pulse observations. The thinner grey line shows the average of the 100 brightest pulses. The profiles have been normalized to have the same peak flux density. Lower panel: pulse-energy histogram for window P, as displayed in uppermost panel. The labels for the panel are the same as in Fig. 2.

to detect jitter noise in observations at 3100 or 730 MHz due to sensitivity limitations of our observations. However, our upper limits were consistent with the analysis at 1400 MHz.

4.6 PSR J1909−3744

At decimetre wavelengths, PSR J1909−3744 shows a narrow 42 μs wide main component and a faint interpulse, with both identified in the upper panel of Fig. 14. Single pulses were detected from the main pulse but not from the interpulse. The average pulse profile formed from the 100 brightest pulses is also displayed in the upper panel of Fig. 14. The profile width is ≈80 per cent of the width of the profile of all the pulses, indicating that, like PSR J1744−1134, and unlike PSR J0437−4715, bright single pulses are emitted across nearly the entire width of the main pulse.

Of all the pulsars in the sample, PSR J1909−3744 deviates the most from a log-normal distribution. The pulse-energy distribution more closely resembles a Gaussian distribution. The energy distribution for a window centred on the main pulse (labelled P in Fig. 14) and its best-fitting generalized Gaussian model are displayed in the bottom panel of Fig. 14. Relative to a Gaussian distribution ($\alpha = 2$ in equation 9), the pulse-energy distribution shows a broader distribution about the mean value (i.e. platykurtic).

This lack of bright pulses contribute to the low levels of jitter noise for the pulsar. The paucity of bright $>5\sigma$ pulses results in small (but measurable) levels of pulse distortion.

Unlike other pulsars in the sample, we find evidence that $\sigma_J(N_p)$ does not scale with a single power law $\propto N_p^{-1/2}$ as would be expected if no temporal correlations between pulses exist. In Fig. 15, we show how σ_{obs} and σ_J scale with N_p. For profiles averaged from

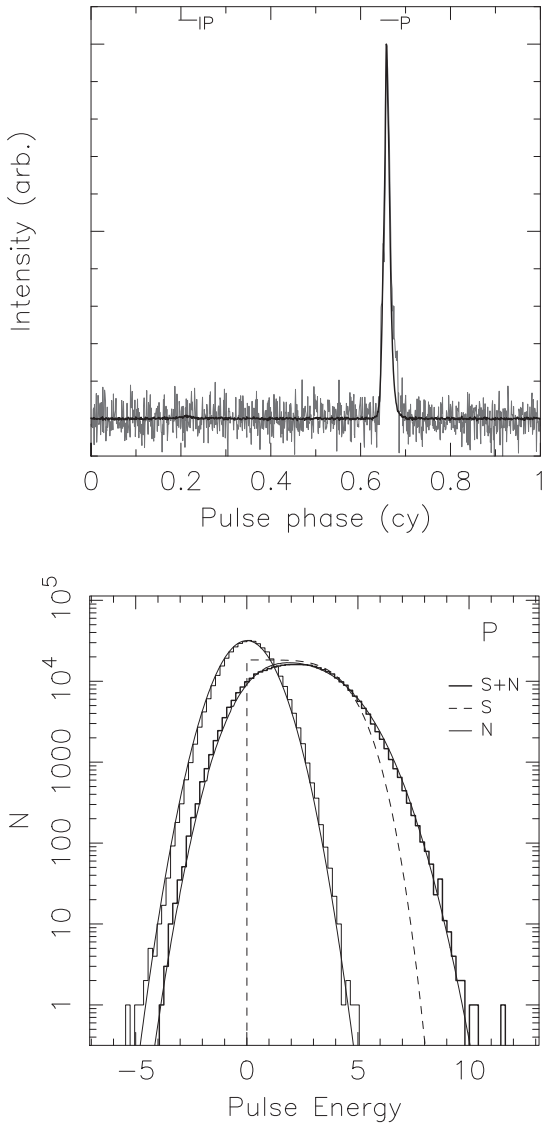

Figure 14. Upper panel: pulse profiles for PSR J1909−3744. The thick line shows the average pulse profile formed from all of our single-pulse observations. The thinner grey line shows the average of the 100 brightest pulses. The profiles have been normalized to have the same peak flux density. Lower panel: pulse-energy distribution in window P for PSR J1909−3744. The labels are the same as in Fig. 2.

much less than 10^3 pulses, and profiles averaged from much longer than 10^3 pulses show $\sigma_J \propto N_p^{-1/2}$, but offset from each other. We searched for periodicities in the pulse energy using two-dimensional fluctuation spectra. We observed excess power at low (but non-zero) fluctuation frequency, but did not find any evidence for periodic features. In Fig. 16, we show residual TOAs formed from averages of 200 pulses. The TOAs show variations that are correlated over 2 s (≈2000 pulses), much shorter than the time-scale of the structure observed in PSR J1713+0747. Power spectral analysis of the residuals shows the presence of power at low fluctuation frequency; however, there is no evidence for significant periodicities.

We estimate that at 1400 MHz, jitter noise contributes approximately 10 ns rms timing error for an hour-long observation, the lowest level of any pulsar in our sample. We were unable to detect the presence of jitter at 3100 or 730 MHz, but the limits on the level of jitter were consistent with observations at other frequencies.

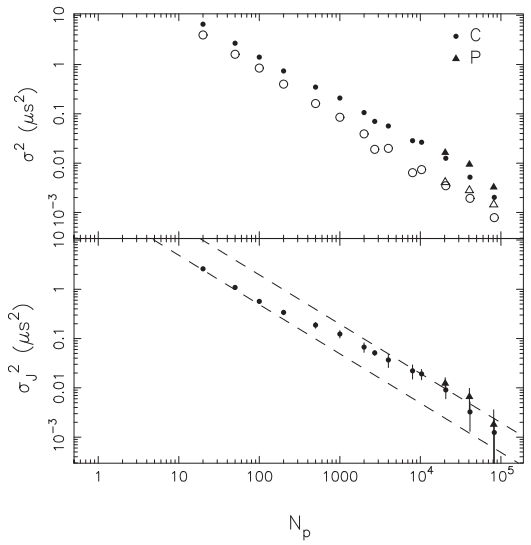

Figure 15. Estimates of levels of jitter noise for PSR J1909−3744. Upper panel: variance of residual time series for observed data sets (filled symbols) and simulated data sets (open symbols). The symbols shapes represent different backends and are listed below. Lower panel: the difference between the observed and simulated variance. We attribute this difference to pulse-shape variations. The dashed lines show the levels of jitter noise predicted from observations of $<10^3$ pulses (lower line) and $>10^4$ pulses (upper line), both scaling $\propto N_p^{-1/2}$. Symbols: circles – CASPSR at 1400 MHz (labelled C); triangles – PDFB3 at 1400 MHz (labelled P).

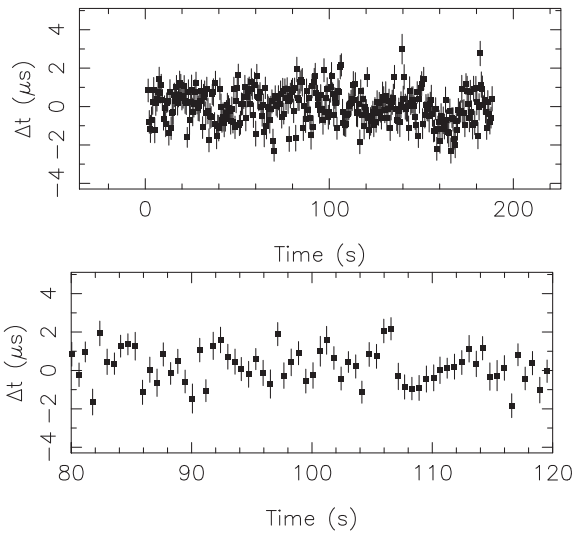

Figure 16. Top panel: residual TOAs for PSR J1909–3744, derived from pulse profiles formed from 200 consecutive pulses. Bottom panel: subinterval that highlights correlated residuals.

4.7 PSR J2145−0750

PSR J2145−0750 has a spin period of ∼15 ms and, at 1400 MHz, the pulsar shows a complex profile morphology, with two strong components (C1 and C2) and a precursor (Pre), as displayed in Fig. 17. We have identified strong pulses centred on both main features. We did not detect any bright pulses from the precursor. A pulse profile formed by adding the 100 brightest pulses, displayed in Fig. 17, shows that the brightest pulses generally originate from the leading component C1.

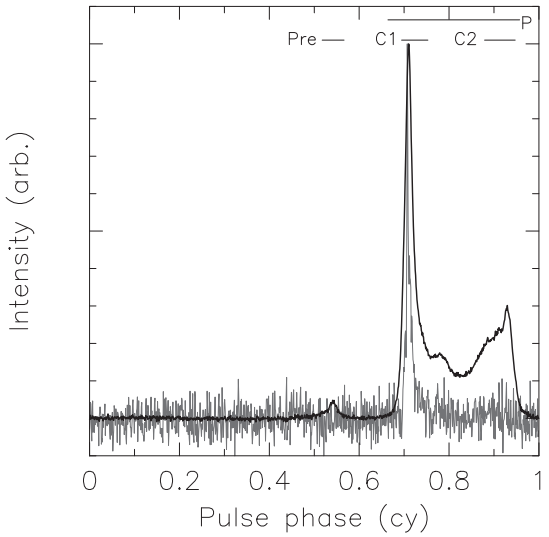

Figure 17. Pulse profiles for PSR J2145−0750. The thick line shows the average pulse profile formed from all of our single-pulse observations. The thinner grey line shows the average of the 100 brightest pulses. The profiles have been normalized to have the same peak flux density.

PSR J2145−0740 shows similar pulse-energy characteristics to other multicomponent pulsars in our sample. The pulse-energy distributions, plotted in Fig. 18, show log-normal statistics. The best-fitting model distributions are displayed in Table 2. We find that the energy distribution in a window C1 around the leading component has larger mean and modulation than the window C2 around the trailing component. in Fig. 19, we show the joint distribution of pulse energies in windows C1 and C2. Because the distributions of the energies are non-Gaussian we use the non-parametric Spearman rank-order correlation coefficient to test the level of correlation. The Spearman correlation coefficient was found to be −0.2. The probability of the null hypothesis (that there is no correlation) was calculated to be 8×10^{-11}, indicating that negative correlation is highly significant.

The variable pulse morphology introduces large levels of jitter noise. We find that $\sigma_J \propto N_p^{-1/2}$ for $N_p < 1.5 \times 10^4$, the largest value we searched. Because of the large pulse width and slow pulse period, the inferred levels of jitter noise are large, contributing ≈190 ns rms timing error for hour-long observations at 1400 MHz. We were able to detect the presence of jitter noise at 3100 and 730 MHz as well. Unlike the other pulsars in the sample the level of jitter noise increases at higher frequency, with the estimated jitter noise largest at 3100 MHz, as displayed in Table 3. At 1400 and 730 MHz, the jitter levels for the pulsar are comparable with each other.

4.8 Other pulsars

We searched for evidence of jitter in other pulsars in the PPTA sample using only fold-mode observations. The analysis was identical to that of the pulsars discussed above. However, we had limited range in N_p over which to search for the $\sigma_J \propto N_p^{-1/2}$ scaling expected of jitter.

We find evidence of S/N-independent noise in the observations of PSR J1939+2134, in observations in both bands at ∼1400 and 730 MHz. In the 1400 MHz band, we associate this with jitter noise. At 730 MHz, we associate this noise with variable (and stochastic) broadening of the pulse profile, referred to as the finite-scintle effect by Cordes & Shannon (2010). Indeed, the effects of stochastic pulse

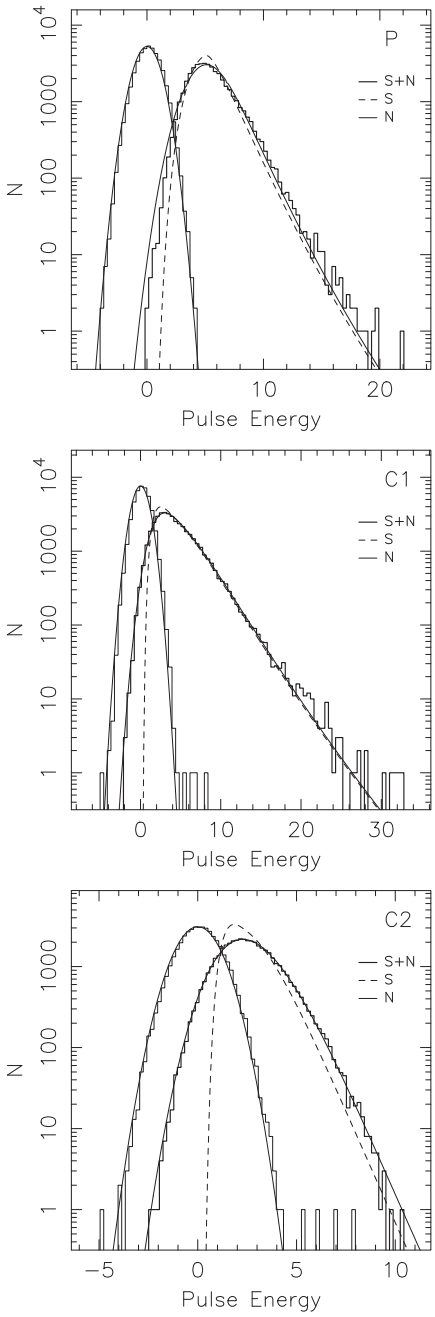

Figure 18. Pulse-energy histograms for PSR J2145−0750. In the uppermost panel, we show the pulse-energy distribution for the main pulse, identified as region P in the upper panel of Fig. 17. In the centre and lowermost panels, we show, respectively, the pulse-energy distribution in windows C1 and C2, also labelled in Fig. 17, centred on components C1 and C2. See Fig. 2 for a description of the plot.

broadening have been measured for this pulsar at 430 MHz (Cordes et al. 1990; Demorest 2011).

At low frequencies, the pulse profile is broadened by multipath propagation through the interstellar medium. The broadening is stochastic, resulting in pulse-shape distortions that affect timing precision. The rms variations of arrival times of Cordes & Shannon (2010) induced by stochastic broadening are

$$\sigma_{\rm DISS} = C_1 \frac{\tau_d}{N_s}, \quad (13)$$

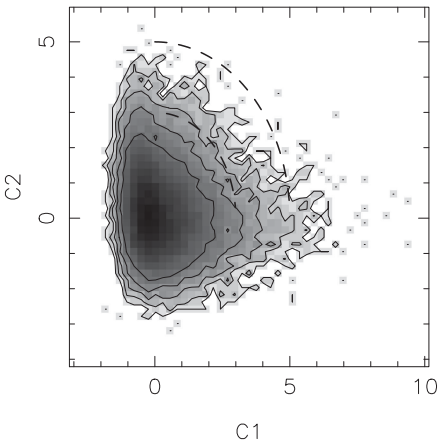

Figure 19. Correlations in energy of components C1 and C2 for PSR J2145−0750. The components have been normalized to have unit mean and variance. The dashed lines show the (1σ) and (2σ) contour of equal probability if component energies are independent.

where τ_d is the pulse broadening time, N_s is the number of scintles in the observation,

$$N_s = \left(1 + \eta \frac{\Delta T}{t_d}\right)\left(1 + \eta \frac{\Delta \nu}{\nu_d}\right), \quad (14)$$

and C_1 is a constant of order unity. In equation (14), ΔT is the observing time, $\Delta\nu$ is the observing bandwidth, ν_d is the diffractive interstellar scintillation (DISS) scale, Δt_d is the diffractive timescale, and η is the filling factor of the scintles. Following convention, $\Delta\nu_d$ is the half-width at half-maximum, and Δt_d is the half-width at the $1/e$ point. Cordes, Weisberg & Boriakoff (1985) found that $\eta \sim 0.2$ and we will assume that value.

In the 1400 MHz band, we find that there is an excess noise with rms amplitude of 40 ns in $T = 30$ s subintegrations, with a bandwidth of 300 MHz. The noise was observed to be uncorrelated from subintegration to subintegration. To estimate the effects of scintillation we calculated the dynamic spectrum of the observation and then formed its two-dimensional autocorrelation function (ACF), measuring its decorrelation time to be $t_d \approx 380$ s, and decorrelation bandwidth to be $\nu_d \approx 1.2$ MHz. Based on these values, we expect that in 30 s subintegrations, stochastic broadening of the pulse profile induces ∼20 ns of rms error, which is a factor of 2 smaller than what is measured. The measured noise is consistent with jitter noise observed in other pulsars, in that the inferred jitter parameter (discussed further below) is in range of values measured for other pulsars in the sample. Higher time resolution observations could be used to distinguish intrinsic shape variations from DISS effects.

There is stronger evidence that our observations at 730 MHz are limited by stochastic broadening. We find that there is time-correlated structure in the residuals that contributes rms scatter of 140 ns to the observations that are correlated over ∼200 s, in subintegrations of 30 s duration. In an analysis of the ACF of the dynamic spectrum, we found $t_d \approx 150$ s and $\nu_d \approx 53$ kHz. We therefore expect stochastic pulse broadening to contribute ∼180 ns rms to observations, which is only 30 per cent larger than the measured values.

We do not expect DISS to play a role in any of the pulsars for which we have detected jitter noise. These pulsars are much more weakly scattered, and even in the 50-cm band, the contribution from scattering is expected to be <10 ns (Coles et al. 2010).

In the remaining pulsars in the sample, we attribute the non-detection of jitter noise to the low flux densities of the pulsars. The effects of jitter are expected to be significant when the instantaneous S/N exceeds unity. We place conservative limits on the level of jitter of the other pulsars by assuming that the jitter contribution to the TOA error is smaller than the total observed rms of the residuals:

$$\sigma_J(N_p) < \sigma_{obs}(N_p). \quad (15)$$

In Table 3, we present measurements of, or limits on, the level of jitter noise in PPTA pulsars. We show both the noise expected at the single-pulse level $\sigma_J(1)$ and in 1 h of observation $\sigma_J(h)$ in addition to the jitter parameter calculated using W_{eff}, W_{50}, and $W_{eff}(1 + m_I^2)$ as measurements of pulse widths.

We measured the correlation of $\sigma_J(1)$ with W_{50}, W_{10}, W_{eff}, $W_{50}(1 + m_I^2)$, and $W_{eff}(1 + m_I^2)$. We find that the strongest correlation is between $\sigma_J(1)$ and $W_{eff}(1 + m_I^2)$. In Fig. 20, we show the relationship between $W_{eff}(1 + m_I^2)$ and $\sigma_J(1)$.

We fitted the relationship $\sigma_J(1) = \bar{f}_J W_{eff}(1 + m_I^2)$, with $\bar{f}_J$ as a free parameter. For pulsars without single-pulse observations, we assume $m_I = 0.3$, though our results were not sensitive to this value. We find that the best-fitting jitter parameter is $\bar{f}_J \approx 0.5$, which is indicated as a solid line Fig. 20. We find that excluding the correction for the modulation index did not change the value $\bar{f}_J$ significantly, and only increased the scatter (and hence decreased the level of correlation). A poor correlation is measured between the effective width $W_{eff,L}$ (see equation 4) and $\sigma_J(1)$. This is not surprising because $W_{eff,L}$ is sensitive to broad components that do not contribute greatly to pulse jitter.

For the other pulsars that we have not detected the presence of jitter noise, we place limits on jitter parameter, and set upper limits $f_J > 0.8$, consistent with the detections of jitter noise and indicating that the non-detections of jitter are associated with insufficient sensitivity.

5 IMPROVING PULSAR TIMING IN THE PRESENCE OF JITTER NOISE

5.1 Including jitter noise in timing models

In pulsar timing observations it is common to account for unknown uncertainties by (1) multiplying the TOA uncertainty by an arbitrary factor (EFAC); (2) adding to the TOA uncertainty an additional term in quadrature (EQUAD); or both (Edwards et al. 2006).

EFACs were originally included in the pulsar timing program TEMPO to account for the fact that the reduced χ^2 of the best-fitting models were typically greater than unity. EQUAD factors were included to avoid overemphasizing high-S/N observations in weighted fits. Overweighted points effectively reduce the number of degrees of freedom for the fit and, in the presence of systematic TOA errors, can easily bias the timing solution.

Common EQUAD or EFAC values are typically applied to all the TOAs in a pulsar timing data set, or to large subsets that are expected to have identical values, such as TOAs derived from the same backend instrument at the same observing radio frequency. Various methods have been used to estimate their values. The most common method is to adjust the values until the reduced χ^2 of the fitted model reaches unity. Bayesian and other maximum likelihood methods have also recently been developed and applied to precision pulsar timing data sets (van Haasteren et al. 2009; Lentati et al. 2014). In these methods, EFAC and EQUAD are included as nuisance parameters and marginalized when calculating the posterior distributions of parameters of interest or comparing models.

Table 3. Jitter noise in PPTA pulsars.

PSR	ν (MHz)	W_{10} (μs)	W_{50} (μs)	$W_{\rm eff}$ (μs)	$W_{{\rm eff},m_{\rm I}}$ (μs)	$\sigma_{\rm J}(1)$ (μs)	$\sigma_{\rm J}$(h) (ns)	$f_{\rm J,\,eff}$	$f_{{\rm J},m_{\rm I}}$	$f_{\rm J,\,50}$
J0437−4715	3100	267	89	44	51	32 ± 1	41 ± 2	0.73 ± 0.02	0.63 ± 0.02	0.36 ± 0.01
	1400	1001	138	76	88	38.0 ± 0.4	48.0 ± 0.6	0.500 ± 0.003	0.434 ± 0.003	0.2762 ± 0.002
	730	1975	233	131	151	48 ± 7	61 ± 9	0.37 ± 0.05	0.32 ± 0.05	0.21 ± 0.03
J1022+1001	3100	1626	371	169	208	130 ± 70	280 ± 140	0.8 ± 0.5	0.6 ± 0.4	0.4 ± 0.2
	1400	1963	969	122	150	134 ± 6	290 ± 15	1.10 ± 0.04	0.89 ± 0.04	0.138 ± 0.006
	730	1873	823	175	215	80 ± 30	70 ± 13	0.5 ± 0.1	0.4 ± 0.1	0.10 ± 0.04
J1603−7202	3100	1579	287	149	192	<277	<560	<2	<1	<0.8
	1400	1723	1210	147	190	146 ± 31	300 ± 56	1.0 ± 0.2	0.8 ± 0.2	0.12 ± 0.03
	730	2020	1342	216	279	<281	<570	<1	<1	<0.2
J1713+0747	3100	380	107	59	64	37 ± 12	40 ± 10	0.6 ± 0.2	0.6 ± 0.2	0.3 ± 0.1
	1400	377	108	63	68	31.1 ± 0.7	35.0 ± 0.8	0.49 ± 0.01	0.46 ± 0.01	0.29 ± 0.01
	730	568	221	126	136	<174	<200	<1	<1	<0.8
J1744−1134	3100	224	97	65	75	<171	<200	<3	<2	<2
	1400	245	138	73	84	35.5 ± 0.7	37.8 ± 0.8	0.49 ± 0.01	0.423 ± 0.009	0.258 ± 0.006
	730	273	150	73	84	<161	<200	<2	<2	<1
J1909−3744	3100	74	35	19	21	<34	<300	<2	<2	<1
	1400	88	42	24	26	10 ± 1	8.6 ± 0.8	0.40 ± 0.04	0.36 ± 0.04	0.23 ± 0.03
	730	110	60	28	31	<61	<60	<2	<2	<1
J1939+2134	3100	859	46	21	23	<73	<48	<3.5	<3.2	<0.08
	1400	854	12	16	17	5 ± 1	6 ± 1	0.3 ± 0.09	0.3 ± 0.1	0.007 ± 0.002
	730	863	820	17	19	19 ± 1	13 ± 1	1.15 ± 0.06	1.03 ± 0.6	0.023 ± 0.001
J2145−0750	3100	4090	350	199	217	200 ± 48	420 ± 99	1.0 ± 0.3	0.9 ± 0.3	0.6 ± 0.1
	1400	4170	340	205	224	91 ± 3	192 ± 6	0.44 ± 0.02	0.407 ± 0.01	0.267 ± 0.009
	730	4194	413	204	223	80 ± 15	170 ± 38	0.40 ± 0.08	0.37 ± 0.06	0.20 ± 0.04
J0613−0200	1400	925	465	43	47	<409	<400	<9	<9	<0.9
J0711−6830	1400	2561	1899	73	80	<71	<90	<1	<0.9	<0.04
J1017−7156	1400	142	72	36	39	<124	<100	<3.4	<3.2	<0.9
J1024−0719	1400	1464	497	65	71	<255	<300	<4	<4	<0.5
J1045−4509	1400	1445	756	274	299	<623	<900	<2	<2	<0.8
J1600−3053	1400	407	93	61	67	<234	<200	<4	<4	<2
J1643−1224	1400	928	319	206	225	<402	<500	<2	<2	<1
J1730−2304	1400	1712	976	97	106	<258	<400	<3	<2	<0.3
J1732−5049	1400	1617	295	171	186	<659	<800	<4	<4	<2
J1824−2452A	1400	1600	979	30	33	<277	<300	<9	<8	<0.2
J1857+0943	1400	3011	523	103	112	<219	<300	<2	<2	<0.4
J1939+2134	1400	859	65	25	27	<15	<10	<0.6	<0.5	<0.2
J2124−3358	1400	876	124	140	153	<341	<400	<2	<2	<3
J2129−5721	1400	617	265	75	82	<386	<400	<5	<5	<1
J2241−5236	1400	123	64	28	31	<58	<50	<2	<2	<0.9

Notes: For each pulsar we list measurements at different observing frequencies. We list the pulse width measured at 10 per cent of peak intensity W_{10}, 50 per cent of peak intensity W_{50}, and the effective pulse width $W_{\rm eff}$, as defined in equation (3). We also list the rms noise expected due to jitter per pulse ($\sigma_{\rm J}(1)$), and expected in an hour-long observation $\sigma_{\rm J}$(h). We calculate the jitter parameter using, $W_{\rm eff}$, W_{50}, and $W_{\rm eff}(1+m_{\rm I}^2)$ as proxies for pulse width. For the pulsars for which we did not measure the modulation index $m_{\rm I}$, we assumed $m_{\rm I}=0.3$.

Instead of modelling the factors EQUAD and EFAC from the timing data sets, we add a term associated with pulse-shape variations, derived from our single-pulse and intraobservation analysis, and not as part of the timing model. We modify the TOA uncertainty $\Delta_{\rm TOA}$ by adding a term to account for pulse jitter:

$$\Delta_{\rm TOA}^2 = \Delta_{\rm F}^2 + \left(\frac{\sigma_{\rm J}}{\sqrt{N_{\rm p}}}\right)^2 = \Delta_{\rm F}^2 + \sigma_{\rm J}^2(1)\frac{P}{T}, \qquad (16)$$

where $N_{\rm p}=T/P$ is the number of co-added pulses, P is the pulse spin period, T is the observing span, $\Delta_{\rm F}$ is the formal TOA uncertainty, and $\sigma_{\rm J}(1)$ is the level of jitter noise expected from a single pulse.

As an example, we analyse a subset of observations for PSR J0437−4715, the brightest MSP in our sample, and one where we expect all of our observations to show evidence for pulse jitter. We use observations conducted in the 10-cm band with the PDFB4 backend taken from the end of its commissioning in 2008 to the end of 2013 (MJDs 54753–56646). We corrected the observations for dispersion measure variations using multifrequency PPTA data and a technique that has been shown not to remove noise from pulsar timing residuals (Keith et al. 2013). In contrast to the PPTA analysis, in which pulse profiles are formed from the invariant interval (Britton et al. 2000), we formed profiles from total intensity (Stokes I parameter). Observations varied from approximately 2 to 64 min in duration, enabling us to compare the correction scheme given in equation (16) to established techniques.

After modifying the TOA uncertainties, the timing model presented in Manchester et al. (2013) was refitted. In Fig. 21, we plot the residual TOAs of this best-fitting model. We find that the weighted rms of the residuals over 5 yr is 64 ns and the reduced χ^2 of this model is 1.1.

We compared the results of this noise model to two alternate cases that have previously been applied to pulsar timing data sets: (a) fitting is conducted with no modification to the TOA uncertainties

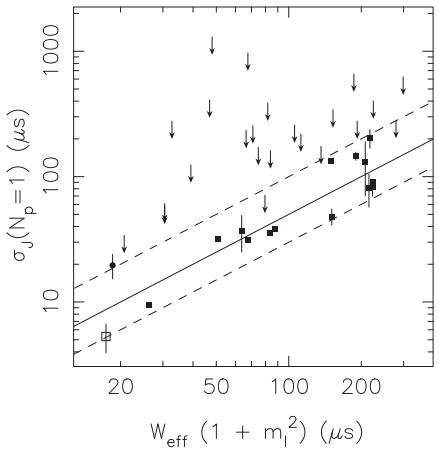

Figure 20. Correlation of pulse width $W_{\rm eff}(1+m_{\rm I}^2)$ and level of jitter noise $\sigma_{\rm J}(N_{\rm p}=1)$. The downward pointing arrows show upper limits on the levels of jitter noise. The lines represent different models $\sigma_{\rm J}=\bar{f}_{\rm J}W_{50}$, where $\bar{f}_{\rm J}$ is the mean value for the relationship. The solid line is the best-fitting value $\bar{f}_{\rm J}=0.5\pm0.1$, the lower and upper dashed lines show the trends $\bar{f}_{\rm J}=0.3$ and 1.0, respectively. The open square shows measurements of jitter noise for PSR J1939+2134 at 1400 MHz, while the filled circle shows excess noise at 730 MHz that we attribute to the effects of stochastic pulse broadening.

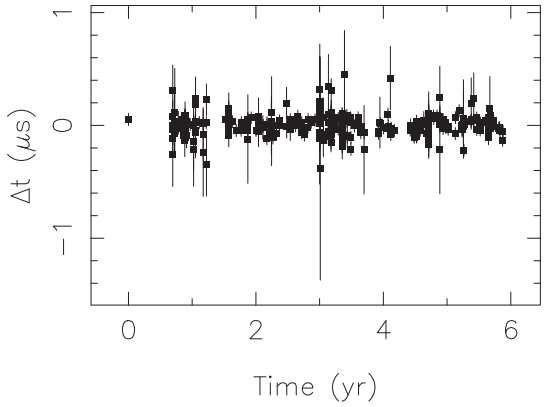

Figure 21. Residual TOAs for PSR J0437−4715. The TOA uncertainties include a term to account for jitter noise.

and, as discussed above, (b) including an EQUAD term such that the reduced χ^2 of the residuals for the best-fitting model is unity. In Fig. 22, we show histograms of the normalized residuals from the three fits, and the normal distribution expected if the uncertainties match the arrival times. In case (a), after fitting, we find that the reduced χ^2 was approximately 8, and the distribution of uncertainties is much broader than expected. In case (b), the added EQUAD factor (panel b) gave a reduced χ^2 of unity; however, the distribution of uncertainties is too narrow. The uncertainties of the high-precision long-integration TOAs have been suppressed to account for outlying short observations present in the observations. Including jitter explicitly (panel c) we find that the normalized TOAs well match the expected distribution. The distribution of the TOA uncertainties best matches a Gaussian distribution.

In order to assess the improvement of our weighting schemes to cases (a) and (b), we produced power spectra of the residuals. In all cases, we found that the power spectra were white. To compare the methods, we measured the amplitude of the power spectral density (PSD). The amplitude of the PSD in our weighting scheme is ∼20 per cent lower than case (a) and ∼27 per cent lower than case

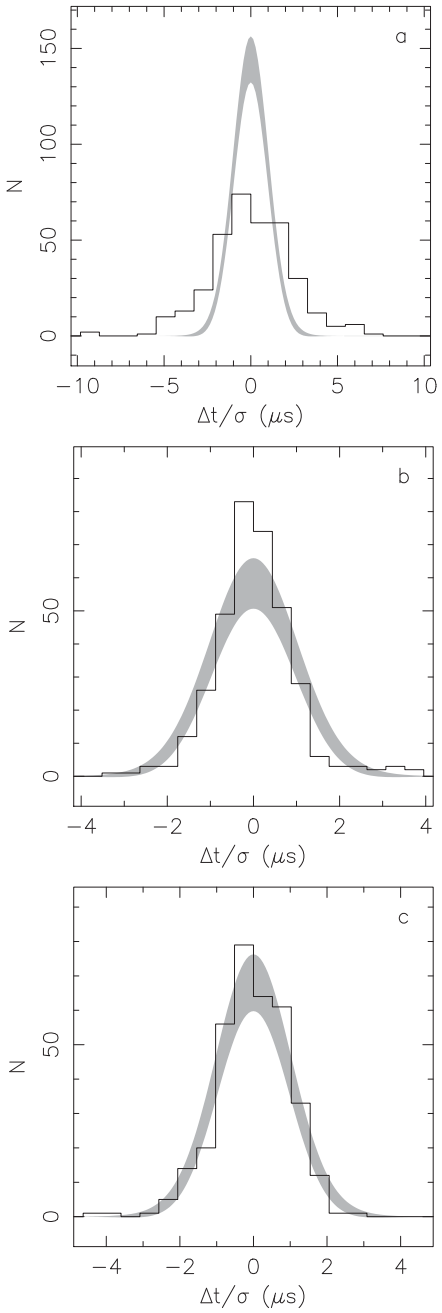

Figure 22. Histograms of normalized residuals for PSR J0437−4715. Panel (a): no modification to TOA uncertainties. Panel (b): adding in quadrature 100 ns to the TOA uncertainties. Panel (c): modifying TOA error using equation (16). The grey shaded area represents the range in the histogram theoretically expected.

(b). This suggests that TOAs weighted using our scheme are more sensitive to the gravitational-wave background (GWB).

We emphasize that we have corrected the error bars using a physically motivated technique that uses an a priori model of the residuals. In addition to providing a better model of the true TOA uncertainties, EQUAD and EFAC parameters may not need to be modelled in timing data sets. This reduces by two the dimensionality to TOA modelling, which streamline computationally intensive Bayesian gravitational-wave-search algorithms (van Haasteren et al. 2009). In archival data, it may be necessary to include EFAC or EQUAD

parameters to account for pulse shape distortions induced by non-linearities in instrumentation associated with low-bit digitization.

5.2 Timing a subselection of pulses

For many pulsars, the brightest pulses originate in a narrow region of pulse phase. Examples of this is are the giant pulses from the MSP PSR J1939+2134, which are emitted in only a narrow window of pulse phase. This suggests that it may be possible to form a more precise TOA by producing a pulse profile from a selection of pulses. Selecting bright pulses comes at a sacrifice of averaging fewer pulses together, exacerbating the effects of any jitter present in the subset. If instead of timing all of the pulses, a fraction f of the $N_{\rm p}$ pulses is used the expected timing precision would be

$$\sigma_{\rm J}(f, N_{\rm p}) = \frac{\sigma_{\rm J}(f, 1)}{\sqrt{f N_{\rm p}}}, \quad (17)$$

where $\sigma_1(f, N_{\rm p})$ is the scatter in the $fN_{\rm p}$ selected single pulses.

From equation (17) we can derive a condition on the timing improvement achieved by using a fraction of the pulses. Improvement is achieved if and only if

$$\sigma_{\rm J}(f, 1) < \sigma_{\rm J}(1, 1)\sqrt{f}. \quad (18)$$

The brightest pulses must originate in a narrow region of pulse phase to achieve an improvement in timing precision.

In order to see if an improvement could be obtained, we tested equation (18) using our fast-sampled observations of PSR J0437−4715 and PSR J1909−3744. We formed profiles from only fractions f of the brightest pulses. We then cross-correlated these profiles with the standard template, and measured the resulting rms of the corresponding time series.

In Fig. 23, we see how $\sigma_{\rm J}$ depends on f for these pulsars. For PSR J0437−4715, the rms error does decrease when selecting only the brightest pulses as the brightest pulses originate from a narrow region of pulse phase. However, it does not decrease sufficiently quickly to warrant timing only the brightest pulses and better timing precision is achieved by timing all of the pulses.

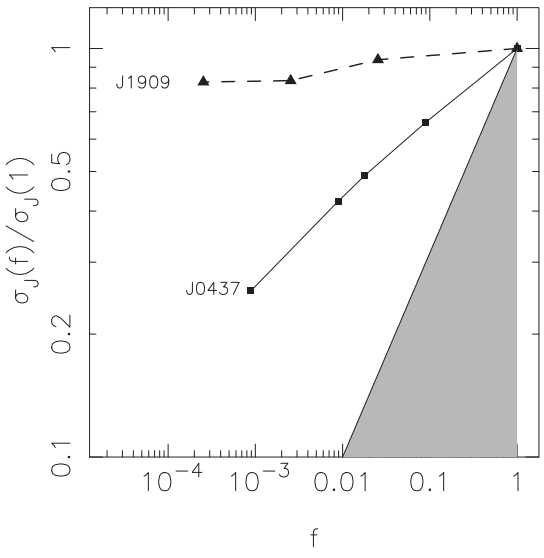

Figure 23. Fraction of pulses used versus normalized timing error for PSR J0437−4715 (labelled J0437) and PSR J1909−3744 (labelled J1909). The filled grey area identifies the region $\sigma_{\rm J}(1, f) < \sigma_{\rm J}(1, 1)/\sqrt{f}$, in which precision timing would benefit from using fewer pulses.

PSR J1909−3744 shows only a modest decrease in the timing error when bright pulses are selected. The rms error in the subselection only reduces to a level of ≈80 per cent of the rms error of all of the pulses. This suggests that bright pulses span a region as nearly as wide as the entire main pulse, consistent with the profile of the brightest pulses (see Fig. 14).

Osłowski et al. (2014) tested both this idea and a related idea of timing only the weakest pulses. In this manner the effects of pulse jitter can be minimized and a better χ^2 of the timing model can be achieved when including only data with instantaneous S/N of less than unity. This yields more realistic formal TOA uncertainties. However, using equation (16) we can now account for pulse jitter and correct the formal TOA uncertainties.

6 DISCUSSION AND CONCLUSIONS

In the highest S/N observations of the MSPs in our sample, we find that there is a contribution to timing uncertainty in excess of what is expected from radiometer noise alone. We attribute this contribution to stochastic shape variations. For PSR J1713+0747, we find an excess that is common to multiple instruments and different telescopes. Our results suggest pulse jitter is a generic property of MSPs (and pulsars in general) and that all MSPs will show jitter if observed with sufficient sensitivity. This is to be expected because the pulsar emission can be thought of as a noise source (Rickett 1975; Osłowski et al. 2011, 2013). We estimate that the rms contribution of jitter is $\sigma_{\rm J}(T) \approx 0.5 W_{\rm eff}\sqrt{P/T}$, where P is the pulse spin period, T is the observing span, and $W_{\rm eff}$ is the effective width defined in equation (3). Because pulse widths typically decrease with higher observing frequencies, we find that jitter noise is lower in the 10-cm band than in the 20- or 50-cm bands.

We find that we can better account for TOA uncertainty when we include in quadrature a jitter noise term extrapolated from our single-pulse estimates. If jitter noise is not properly included in the timing model (either being ignored or through an erroneously applied EQUAD) the longer lower gain observations from smaller telescopes will be improperly down weighted.

Consistent with previous observations, we find that jitter noise is correlated within observing bands. For PSR J0437−4715 there is sufficient S/N to detect jitter noise simultaneously at both 730 and 3100 MHz in the dual band 10-cm/50-cm receiver. While jitter noise is present in both bands, it is uncorrelated between the bands. Either the pulse emission decorrelates between the bands or the components contributing the jitter noise are different. Over wide bandwidths pulsar emission has varying levels of correlation, with some pulsars showing high levels of correlation in pulse energy over 3 GHz bandwidth (Bartel & Sieber 1978), others showing little correlation between 0.08 and 1.4 GHz (Robinson et al. 1968), and others showing intermediate behaviour (Bhat et al. 2007). Dual-band single-pulse data sets for PSR J0437−4715 would enable better characterization of the nature of the correlation of the pulse shape variations. For the other pulsars in the sample, the dual frequency analysis was not possible because they do not have the sensitivity to detect jitter noise simultaneously in both bands of the 10-cm/50-cm receiver. Such analysis would be feasible with more sensitive telescopes, if they are equipped with dual-band or broad-band receiving systems.

If jitter noise decorrelates over finite bandwidth, it is possible to mitigate its effects with sufficiently wide-band instrumentation. Many future receiving systems will have wide bandwidths, sampling from a frequency range of ∼0.5–4 GHz of great utility for pulsar timing. These systems may sample a few independent realizations

of jitter, reducing its rms contribution to overall timing uncertainty. However, the decorrelation may introduce a bias if a single-epoch dispersion variation correction strategy is employed (Demorest et al. 2013) because the frequency-dependent shape variations may be interpreted as dispersion measure variations (Pennucci et al. 2014).

We find that most of the MSPs for which we could detect single pulses show log-normal pulse-energy distributions. Our pulse-energy statistics show similarities to slower pulsars. In a sample of ≈350 pulsars, Burke-Spolaor et al. (2012) found that the majority showed log-normal or nearly log-normal energy distributions, with a minority showing Gaussian energy distributions. We find no evidence for power-law pulse-energy distributions or giant pulses in our single-pulse observations. The pulsar that has the lowest level of jitter noise, PSR J1909−3744, does not show evidence for a log-normal tail in pulse energies, which results in a relatively low level of jitter noise. Cairns et al. (2004) found that in the slowly spinning pulsars in their study, the edges of the pulse profiles show Gaussian energy modulation. The edges of the pulse were interpreted as arising from the edge of the open field line region. This suggests, that for PSR J1909−3744, our line of sight may traverse the edge of an emission region.

We have not explored algorithms for correcting data sets for pulse-shape variability. In order for this to work it is necessary to find a strong correlation between the pulse shape and another measurable quantity of interest, because the error in the correction will be $\propto 1 - \rho^2$, where ρ is the correlation coefficient (Cordes & Shannon 2010). Osłowski et al. (2011, 2013) have identified methods to correct for pulse shape variability in PSR J0437−4715, reducing the rms of the residuals by 20–40 per cent. Shannon & Cordes (2012) identified only a weak correlation between pulse arrival time and S/N in PSR J1713+0747. The level of correlation was insufficient to implement a correction scheme.

We also have not explored optimal intraobservation weighting schemes. Typically pulse profiles are formed, after removing RFI and calibrating, combining the many subintegrations. These subintegrations are typically combined using natural weighting, with the higher S/N portions of the observations given greater weight. If a pulsar is in a jitter-dominated state (at least in the brightest observations), this scheme overweights the brightest portion of the observation. This reduces the effective number of pulses in the profile. To mitigate this effect TOAs could be produced from shorter subintegrations and the errors corrected using equation (16). Another possibility would be to combine the subintegration using a weighting scheme that accounts for the presence of S/N independent noise.

These results are relevant to PTA activities on current and future telescopes. It is important to incorporate the effects of jitter when considering the sensitivity of pulsar timing array experiments to gravitational waves (Cordes & Shannon 2012), and to optimize observing strategies. Based on our results, we expect that pulse-shape variations limit the timing precision at the larger aperture telescopes that are part of the North American Nanohertz Observatory for Gravitational Waves (NANOGrav; Demorest et al. 2013) and the European Pulsar Timing Array (EPTA; Ferdman et al. 2010). Observations of bright MSPs made using very long baseline interferometry with the Large European Array for Pulsars (LEAP; Kramer & Champion 2013), which has a sensitivity comparable to Arecibo, will also be limited by jitter noise. Including an improved noise model is especially important for producing data sets from observations with different integration times, such as for the International Pulsar Timing Array (IPTA) project (Hobbs et al. 2010), which combines EPTA, NANOGrav, and PPTA data. The IPTA data sets contain short-integration high-sensitivity TOAs from large-aperture telescopes that need to be properly combined with less sensitive longer integration observations. As such, if the effects are not incorporated in the timing analysis, a modest loss in sensitivity to the GWB would be expected. The IPTA project could also consider alternative scheduling strategies in which the smaller aperture telescopes focus on the bright pulsars that would be jitter dominated when observed at larger aperture telescopes. The larger telescopes could then focus on fainter pulsars.

The IPTA pulsars will all be candidates for PTA observations with MeerKAT, the Five Hundred Metre Aperture Spherical Telescope (FAST), and the Square Kilometre Array (SKA). These telescopes will all have larger collecting area than the Parkes telescope. Observations with these telescopes are likely to be jitter noise limited for many of these pulsars. Subarray modes in which the array can be split and observe multiple pulsars independently would maximize the timing throughput. Alternatively, in the era of the SKA, the brighter timing array pulsars could be observed with 100-m class radio telescopes.

ACKNOWLEDGEMENTS

We thank the referee for helpful comments that improved the clarity of the text. The Parkes radio telescope is part of the Australia Telescope National Facility which is funded by the Commonwealth of Australia for operation as a National Facility managed by CSIRO. This work was performed on the gSTAR national facility at Swinburne University of Technology. gSTAR is funded by Swinburne and the Australian Government's Education Investment Fund. This work was supported by the Australian Research Council through grant DP140102578. GH is a recipient of a Future Fellowship from the Australian Research Council. VR is a recipient of a John Stocker post-graduate scholarship from the Science and Industry Endowment Fund of Australia. LW acknowledges support from the Australian Research Council. This work made use of NASA's ADS system.

REFERENCES

Ables J. G., McConnell D., Deshpande A. A., Vivekanand M., 1997, ApJ, 475, L33
Antoniadis J. et al., 2013, Science, 340, 448
Bartel N., Sieber W., 1978, A&A, 70, 307
Bhat N. D. R., Gupta Y., Kramer M., Karastergiou A., Lyne A. G., Johnston S., 2007, A&A, 462, 257
Britton M. C., van Straten W., Bailes M., Toscano M., Manchester R. N., 2000, in Kramer M., Wex N., Wielebinski R., eds, ASP Conf. Ser. Vol. 202, IAU Colloq. 177, Pulsar Astronomy – 2000 and Beyond. Astron. Soc. Pac., San Francisco, p. 73
Burke-Spolaor S. et al., 2012, MNRAS, 423, 1351
Cairns I. H., Robinson P. A., Das P., 2002, Phys. Rev. E, 66, 066614
Cairns I. H., Johnston S., Das P., 2004, MNRAS, 353, 270
Champion D. J. et al., 2010, ApJ, 720, L201
Coles W. A., Rickett B. J., Gao J. J., Hobbs G., Verbiest J. P. W., 2010, ApJ, 717, 1206
Cordes J. M., Downs G. S., 1985, ApJS, 59, 343
Cordes J. M., Shannon R. M., 2010, ApJ, preprint (arXiv:1010.3785)
Cordes J. M., Shannon R. M., 2012, ApJ, 750, 89
Cordes J. M., Weisberg J. M., Boriakoff V., 1985, ApJ, 288, 221
Cordes J. M., Wolszczan A., Dewey R. J., Blaskiewicz M., Stinebring D. R., 1990, ApJ, 349, 245
Demorest P. B., 2011, MNRAS, 416, 2821
Demorest P. B., Pennucci T., Ransom S. M., Roberts M. S. E., Hessels J. W. T., 2010, Nature, 467, 1081

Demorest P. B. et al., 2013, ApJ, 762, 94
Detweiler S., 1979, ApJ, 234, 1100
Downs G. S., Reichley P. E., 1983, ApJS, 53, 169
Edwards R. T., Stappers B. W., 2003, A&A, 407, 273
Edwards R. T., Hobbs G. B., Manchester R. N., 2006, MNRAS, 372, 1549
Ferdman R. D. et al., 2010, Classical Quantum Gravity, 27, 084014
Foster R. S., Backer D. C., 1990, ApJ, 361, 300
Gregory P. C., 2005, Bayesian Logical Data Analysis for the Physical Sciences: A Comparative Approach with 'Mathematica' Support. Cambridge Univ. Press, Cambridge
Groth E. J., 1975, ApJS, 29, 453
Helfand D. J., Manchester R. N., Taylor J. H., 1975, ApJ, 198, 661
Hellings R. W., Downs G. S., 1983, ApJ, 265, L39
Hobbs G. et al., 2010, Classical Quantum Gravity, 27, 084013
Hobbs G. et al., 2012, MNRAS, 427, 2780
Hotan A. W., Bailes M., Ord S. M., 2004a, MNRAS, 355, 941
Hotan A. W., van Straten W., Manchester R. N., 2004b, Publ. Astron. Soc. Aust., 21, 302
Jenet F. A., Gil J., 2004, ApJ, 602, L89
Jenet F. A., Anderson S. B., Kaspi V. M., Prince T. A., Unwin S. C., 1998, ApJ, 498, 365
Jenet F. A., Anderson S. B., Prince T. A., 2001, ApJ, 546, 394
Keith M. J. et al., 2013, MNRAS, 429, 2161
Knight H. S., Bailes M., Manchester R. N., Ord S. M., 2005, ApJ, 625, 951
Kramer M., Champion D. J., 2013, Classical Quantum Gravity, 30, 224009
Kramer M. et al., 1999, ApJ, 520, 324
Kramer M. et al., 2006, Science, 314, 97
Lentati L., Alexander P., Hobson M. P., Feroz F., van Haasteren R., Lee K. J., Shannon R. M., 2014, MNRAS, 437, 3004
Liu K., Keane E. F., Lee K. J., Kramer M., Cordes J. M., Purver M. B., 2012, MNRAS, 420, 361
Lyne A., Hobbs G., Kramer M., Stairs I., Stappers B., 2010, Science, 329, 408
McKinnon M. M., 2004, ApJ, 606, 1154
Manchester R. N. et al., 2013, Publ. Astron. Soc. Aust., 30, 17
Melatos A., Link B., 2014, MNRAS, 437, 21
Osłowski S., van Straten W., Hobbs G. B., Bailes M., Demorest P., 2011, MNRAS, 418, 1258
Osłowski S., van Straten W., Demorest P., Bailes M., 2013, MNRAS, 430, 416
Osłowski S., van Straten W., Bailes M., Jameson A., Hobbs G., 2014, MNRAS, 441, 3148
Pennucci T. T., Demorest P. B., Ransom S. M., 2014, ApJ, preprint (arXiv:1402.1672)
Rickett B. J., 1975, ApJ, 197, 185
Rickett B. J., 1990, ARA&A, 28, 561
Robinson B. J., Cooper B. F. C., Gardiner F. F., Wielebinski R., Landecker T. L., 1968, Nature, 218, 1143
Scheuer P. A. G., Williams P. J. S., 1968, ARA&A, 6, 321
Shannon R. M., Cordes J. M., 2010, ApJ, 725, 1607
Shannon R. M., Cordes J. M., 2012, ApJ, 761, 64
Shannon R. M. et al., 2013a, Science, 342, 334
Shannon R. M. et al., 2013b, ApJ, 766, 5
Siemens X., Ellis J., Jenet F., Romano J. D., 2013, Classical Quantum Gravity, 30, 224015
Stinebring D. R., Cordes J. M., Rankin J. M., Weisberg J. M., Boriakoff V., 1984, ApJS, 55, 247
Taylor J. H., 1992, R. Soc. Lond. Philos. Trans. Ser. A, 341, 117
van Haasteren R., Levin Y., McDonald P., Lu T., 2009, MNRAS, 395, 1005
van Straten W., 2004, ApJS, 152, 129
van Straten W., 2013, ApJS, 204, 13
van Straten W., Bailes M., 2011, Publ. Astron. Soc. Aust., 28, 1
Wolszczan A., Frail D. A., 1992, Nature, 355, 145

This paper has been typeset from a TEX/LATEX file prepared by the author.